

The halo mass function and filaments in full cosmological simulations with fuzzy dark matter

Simon May^{1*} and Volker Springel¹

¹Max-Planck-Institut für Astrophysik, Karl-Schwarzschild-Straße 1, 85741 Garching, Germany

Accepted XXX. Received YYY; in original form ZZZ

ABSTRACT

Fuzzy dark matter (FDM) is a dark matter candidate consisting of ultra-light scalar particles with masses around 10^{-22} eV/ c^2 , a regime where cold bosonic matter behaves as a collective wave rather than individual particles. It has increasingly attracted attention due to its rich phenomenology on astrophysical scales, with implications for the small-scale tensions present within the standard cosmological model, Λ CDM. Although constraints on FDM are accumulating in many different contexts, very few have been verified by self-consistent numerical simulations. We present new large numerical simulations of cosmic structure formation with FDM, solving the full Schrödinger–Poisson (SP) equations using the AXI_{REPO} code, which implements a pseudo-spectral numerical method. Combined with our previous simulations, they allow us to draw a four-way comparison of matter clustering, contrasting results (such as power spectra) for each combination of initial conditions (FDM vs. CDM) and dynamics (Schrödinger–Poisson vs. N -body). By disentangling the impact of initial conditions and non-linear dynamics in this manner, we can gauge the validity of approximate methods used in previous works, such as ordinary N -body simulations with an FDM initial power spectrum. Due to the comparatively large volume achieved in our FDM simulations, we are able to measure the FDM halo mass function from full wave simulations for the first time, and compare to previous results obtained using analytic or approximate approaches. We find that, due to the cut-off of small-scale power in the FDM power spectrum, haloes are linked via continuous, smooth, and dense filaments throughout the entire simulation volume (unlike for the standard Λ CDM power spectrum), posing significant challenges for reliably identifying haloes. We also investigate the density profiles of these filaments and compare to their Λ CDM counterparts.

Key words: dark matter – large-scale structure of Universe – cosmology: theory – galaxies: haloes – methods: numerical – software: simulations

1 INTRODUCTION

A number of tensions between theory and observations on small cosmological scales, such as the ‘cusp–core problem’, the ‘missing satellite problem’, or the ‘too-big-to-fail problem’ (Weinberg et al. 2015; Del Popolo & Le Delliou 2017; Boylan-Kolchin et al. 2011) have sometimes raised questions about the validity of the ‘standard cosmological model’ based on cold dark matter and a cosmological constant (Λ CDM), which has otherwise been extremely successful in describing a wide variety of cosmological observations across a broad range of physical scales (e.g. Frenk & White 2012; Bull et al. 2016). Distinguishing effects due to baryonic physics from genuine failures of Λ CDM has proven to be a significant challenge, however (e.g. Santos-Santos et al. 2020; Grand et al. 2021; Sales et al. 2022). Further, cold dark matter (CDM) as a model only makes predictions in the context of cosmology, with countless possible implementations of galaxy formation physics (see Vogelsberger et al. 2020, for a recent review).

Although large-scale structure studies have solidified the correspondence of observations with the behaviour of CDM, dark matter models can still deviate on less well constrained, smaller (i. e. galactic)

scales. In this regard, fuzzy dark matter (FDM) offers a wide range of new phenomena which have an impact on some of the ‘small-scale problems’ (see e. g. Marsh 2016; Hui et al. 2017; Niemeyer 2020; Hui 2021; Ferreira 2021, for reviews). Due to the small particle masses, interesting wave effects occur which are unique to this class of dark matter models. Early numerical simulations have already shown that ultra-light scalars form cores in the centres of dark matter haloes (Schive et al. 2014), possibly explaining observed dwarf galaxy rotation curves (but see Burkert 2020). In addition, the cut-off in the FDM transfer function, suppressing small-scale power in a similar fashion as warm dark matter (WDM), has the potential to solve issues like the ‘missing satellite problem’. In a sense, FDM combines properties similar to the features of WDM (suppression on small scales) and self-interacting dark matter (SIDM) (cored density profiles) with respect to the small-scale challenges mentioned above (Boyarsky et al. 2019; Tulin & Yu 2018).

However, FDM also exhibits a number of additional unique phenomena. Objects other than cores, such as quantized vortices, are another differentiating feature with interesting prospects for detection (Hui et al. 2021), and relative fluctuations of order one in the density field at the scale of the FDM wavelength can have a strong impact on visible matter e. g. through dynamical heating. Furthermore, light (pseudo-)scalar particles are a common feature of theories in

* E-mail: simon.may@mpa-garching.mpg.de

particle physics, from the original axion in quantum chromodynamics (QCD) to a plethora of axion-like particles predicted by unified and early-universe theories such as string theories (Marsh 2016).

After FDM garnered great interest due to motivation from astrophysics and particle physics, as summarised above, constraints on the mass m of the scalar particles at values around $mc^2 \gtrsim 10^{-21}$ eV accumulated using many different contexts and observables for some time (Ferreira 2021). It has turned out that the scaling relations of FDM halo cores are difficult to reconcile with observations when assuming a single value for the particle mass m (Burkert 2020), and although this does not rule out FDM as a dark matter candidate by itself, it does weaken its motivation as a possible solution to the ‘cusp–core problem’. Relatedly, recent results from dynamical modelling of ultra-faint dwarf (UFD) galaxies (where FDM cores become increasingly large) has been used to claim rather strong constraints on m , with values up to $\approx 10^{-19}$ eV (Hayashi et al. 2021; Zoutendijk et al. 2021). However, these analyses do not take the significant scatter in the FDM core–halo mass relation, discovered in cosmological simulations, into account (Chan et al. 2022), which would weaken these bounds. A very recent result from Dalal & Kravtsov (2022), claiming $mc^2 > 3 \times 10^{-19}$ eV due to the heating effect of stellar orbits caused by potential fluctuations in FDM haloes, has more serious implications, since it does not depend on the uncertain core–halo relation.

However, most of these constraints (including the most recent) have in common that they have not yet been verified by self-consistent numerical simulations, instead relying on approximate, idealised, or simplified numerical and analytic approaches. While cosmological FDM simulations have been carried out using a variety of numerical methods, many attempts were quite limited in scope (Zhang et al. 2018a; Laguë et al. 2021, table 1), so that the effects of FDM in (mildly) non-linear regimes of structure formation are still poorly understood compared to CDM.

Apart from an overall still lower level of research attention, an important reason impeding insight into FDM lies in the very large computational costs incurred when numerically solving the corresponding equations of motion – these costs are much higher than the ones associated with corresponding Λ CDM calculations. Due to the computational requirements, the cosmological volumes studied in simulations with the full FDM Schrödinger–Poisson (SP) dynamics have been especially limited (Woo & Chiueh 2009; Schive et al. 2014; Veltmaat et al. 2018; Mocz et al. 2020). Although recent advances in hybrid numerical techniques have made it feasible to embed simulated FDM haloes within much larger simulated boxes (Schwabe & Niemeyer 2022), the fundamental issues driving the cost in the regions where the full FDM equations of motion are treated remain. In this work, we carry out simulations that smoothly connect the non-linear state reached in isolated FDM haloes to the still linear large-scale structure, thereby bridging, in particular, the regime of mildly non-linear evolution where differences in the temporal evolution compared to CDM can be expected. We complement our previous simulations (May & Springel 2021) by including the self-consistent transfer function expected for an FDM cosmology. As before, we carry out very large FDM simulations with a spectral method on a uniform grid, which fully retains the quantum-mechanical effects. We compare and contrast with our previous results for central measures of matter clustering, namely the power spectrum and the halo mass function (HMF), and highlight the unique challenges and phenomena related to filaments which arise when using an FDM initial power spectrum.

While methods which forego a treatment of the full wave dynamics have been able to conduct simulations with volumes much closer

to those attainable using traditional N -body and smoothed-particle hydrodynamics (SPH) approaches for CDM (Schive et al. 2016; Veltmaat & Niemeyer 2016; Zhang et al. 2018b; Nori & Baldi 2018; Nori et al. 2019; Nori & Baldi 2021), these do not capture inherent wave phenomena such as interference effects, which can have a significant impact on the overall evolution at least on small scales (Li et al. 2019), leaving the validity of results obtained in this way unclear in the absence of similar computations solving the fundamental wave equations. While the hybrid method from Schwabe & Niemeyer (2022) improves upon the computational limitations, by its nature it also does not incorporate the full FDM evolution, and can only reproduce it in a statistical sense. In particular, while all simulations can easily incorporate the impact of the suppressed small-scale power spectrum present with FDM in the initial conditions, such methods either lack the wave nature of FDM entirely or only approximate it. Using our simulations, we are now equipped to fully clarify the reliability of such approximative results, disentangling the two essential physical differences distinguishing FDM from CDM in cosmological numerical simulations: the dynamics (equations of motion) and the initial conditions (ICs).

The paper is structured as follows. In section 2, we concisely summarize the theoretical background of FDM cosmologies, while in section 3 we detail our numerical methodology. In section 4 we compare matter clustering in FDM and CDM cosmologies at the level of the power spectrum, for different sets of initial conditions. We then turn in section 5 to a discussion of the challenges involved in measuring the halo mass function in self-consistent cosmological FDM simulation. In section 6 we consider the density structure of filaments in FDM as compared to CDM, while we return to halo profiles in section 7. Finally, we present a summary of our findings and our conclusions in section 8.

2 THEORETICAL BACKGROUND

Fuzzy dark matter is a particular form of scalar field dark matter with an ‘unusual’ choice of the scalar field particle mass m . It is described by the simple scalar field action

$$S = \frac{1}{\hbar c^2} \int d^4x \sqrt{-g} \left(\frac{1}{2} g^{\mu\nu} (\partial_\mu \phi(x)) (\partial_\nu \phi(x)) - \frac{1}{2} \frac{m^2 c^2}{\hbar^2} \phi(x)^2 - \frac{\lambda}{\hbar^2 c^2} \phi(x)^4 \right), \quad (1)$$

with the metric $g^{\mu\nu}$ and its determinant g , a real scalar field ϕ , its mass m , and a self-interaction coupling strength λ .¹ In this most fundamental description of quantum field theory in a curved spacetime, ϕ is a quantum field. This action is to be understood in the context of quantum field theory in a curved spacetime, i. e. ϕ is a (‘second-quantised’) quantum field, although for the purposes of numerical calculations, we will only consider the ‘classical’ and non-relativistic limits. As in May & Springel (2021), we will not consider self-interactions, i. e. $\lambda = 0$.

As mentioned above, the distinguishing feature of the FDM model is the value of the mass m , which is around $mc^2 \approx 10^{-22}$ eV, making this an *ultra-light* scalar field. This is in stark contrast to most realizations of CDM, such as weakly interacting massive particle (WIMP) models (which include scalar field dark matter models), which feature particle masses in the range of 100 GeV–TeV. A consequence of this wildly

¹ c and \hbar are the speed of light in vacuum and the reduced Planck constant, and are explicitly included in all equations.

different mass regime is that the FDM scalar field is better described as waves instead of individual particles, making FDM an example of a *wave dark matter* model, with associated striking differences in phenomenology. The reason is that, for such ultra-light values of the particle mass, the resulting particle number densities are extremely large, such that the quantum-mechanical de Broglie wavelength will be much larger than the inter-particle separation. Correspondingly, a collective wave description becomes much more appropriate than dealing with individual particles. Notice that such dark matter models require a non-thermal production mechanism to remain ‘cold’, in which case bosons (like the scalar particles of FDM) can form a Bose–Einstein condensate.

As mentioned above, we will assume non-relativistic approximations appropriate for simulations of cosmic structure formation, where all velocities are $\ll c$, and the considered scales are smaller than the Hubble horizon c/H_0 . Rewriting the real scalar field ϕ in terms of a complex variable ψ ,

$$\phi = \frac{1}{2} \sqrt{\frac{\hbar^3 c}{2m}} \operatorname{Re} \left(\psi e^{-i \frac{mc^2}{\hbar} t} \right) = \sqrt{\frac{\hbar^3 c}{2m}} \left(\psi e^{-i \frac{mc^2}{\hbar} t} + \psi^* e^{i \frac{mc^2}{\hbar} t} \right), \quad (2)$$

and taking the non-relativistic limit in the Newtonian gauge yields the equations of motions for fuzzy dark matter, the SP equations:²

$$i\hbar \partial_t \psi(t, \mathbf{x}) = -\frac{\hbar^2}{2ma(t)^2} \nabla^2 \psi(t, \mathbf{x}) + \frac{m}{a(t)} \Phi \psi(t, \mathbf{x}), \quad (3)$$

$$\nabla^2 \Phi(t, \mathbf{x}) = 4\pi G m \left(|\psi(t, \mathbf{x})|^2 - \langle |\psi|^2 \rangle(t) \right), \quad (4)$$

where a is the cosmological scale factor, Φ is the Newtonian gravitational potential, G is Newton’s constant, and the angle brackets in $\langle |\psi|^2 \rangle$ indicate a spatial average. These are the equations of motions whose non-linear time evolution is solved in our numerical simulations. In the above, all quantities and coordinates are given in ‘comoving’ form, to factor out the dependence on the scale factor $a(t)$ as much as possible.³ Explicitly, comoving and ‘physical’ quantities are related as follows:

$$\mathbf{x} = a^{-1} \mathbf{x}_{\text{phys}}, \quad \nabla = a \nabla_{\text{phys}}, \quad \psi = a^{3/2} \psi_{\text{phys}}, \quad \Phi = a \Phi_{\text{phys}}. \quad (5)$$

As we have assumed a production mechanism that can be described as a Bose–Einstein condensate, with almost all of the scalar particles in their quantum-mechanical single-particle ground states and large number densities, we can make use of the mean field approximation, also called the ‘classical’ limit or wave limit, where the particles behave collectively and coherently. The ‘wave function’ ψ in eq. (3), which is now simply a complex number-valued function (instead of a quantum field), is then understood as the single macroscopic amplitude of the FDM waves, with the mass density given by

$$\rho = m |\psi|^2. \quad (6)$$

This is why FDM is often called a ‘classical theory’.⁴

² Since eq. (3), despite being formally identical to the Schrödinger equation from single-particle quantum mechanics, has a very different physical meaning and is in fact a Gross–Pitaevskii equation (Gross 1961; Pitaevskii 1961), eqs. (3) and (4) are technically the Gross–Pitaevskii–Poisson system of equations. However, we will use the more common term ‘Schrödinger–Poisson equations’ here.

³ All quantities will be given in terms of comoving lengths unless specified otherwise.

⁴ The distinction is irrelevant for the physical and phenomenological consequences of FDM, but often seems to spark debate. We would like to note that, although FDM may be described by what is formally a classical field theory, the underlying *physical* phenomena, such as matter waves and Bose–Einstein condensation, were not known in classical physics.

As in quantum mechanics, or generally for diffusion equations, eq. (3) obeys the continuity equation

$$\partial_t \rho + \nabla \cdot \rho \mathbf{v} = 0, \quad (7)$$

with the momentum density

$$\rho \mathbf{v} = \frac{\hbar}{2i} (\psi^* \nabla \psi - \psi \nabla \psi^*). \quad (8)$$

The momentum density $\rho \mathbf{v}$ can also be used to define the bulk peculiar velocity field \mathbf{v} , although this is problematic in the case of $\rho = 0$. Separating the complex wave amplitude ψ into its absolute value $\sqrt{\rho/m}$ and complex phase θ ,

$$\psi = \sqrt{\frac{\rho}{m}} e^{i\theta}, \quad (9)$$

yields a simpler form of eq. (8):

$$\mathbf{v} = \frac{\hbar}{m} \nabla \theta, \quad (10)$$

i. e. the velocity is given by the gradient of the wave amplitude’s phase. Again, however, this is ill-defined when $\psi = \rho = 0$, in which case the phase θ is undefined. It should be noted that due to the presence of wave interference, the case $\psi = 0$ is actually quite common (occurring wherever destructive interference takes place) and cannot be neglected as perhaps for non wave-like dark matter models.

In addition to the mass (as implied by the continuity equation, eq. (7)), the total energy, given by

$$\begin{aligned} E &= \int d^3x \left(\frac{\hbar^2}{2m^2} |\nabla \psi|^2 + \frac{1}{2} \Phi |\psi|^2 \right) \\ &= \int d^3x \frac{\hbar^2}{2m^2} (\nabla \sqrt{\rho})^2 + \int d^3x \frac{1}{2} \rho v^2 + \int d^3x \frac{1}{2} \rho \Phi \\ &= T_\rho + T_v + V \end{aligned} \quad (11)$$

is conserved (Mocz et al. 2017). The kinetic energy $T = T_\rho + T_v$ is made up of the ‘bulk’ kinetic energy T_v , and a gradient energy term T_ρ , while V is the standard gravitational potential energy.

The separation of the wave amplitude into two real variables and their connection with the density (6) and velocity (10) allows a hydrodynamical interpretation analogous to that of Madelung (1927) in quantum mechanics, although its validity is problematic for destructive interference. FDM’s resistance against gravitational collapse on small scales, which can be interpreted as an analogue to the Heisenberg uncertainty principle in the SP formulation, then manifests itself as an explicit additional ‘quantum pressure’ appearing in the analogue of the hydrodynamical Euler equation.

There are two important length scales which serve as indicators of FDM wave phenomena, both of which are determined by the constant \hbar/m , which is the only independent parameter in the equations of motion, eqs. (3) and (4). The first is the de Broglie wavelength

$$\lambda_{\text{dB}} = \frac{2\pi\hbar}{mv}, \quad (12)$$

which has the same meaning as in quantum mechanics and indicates the length scale on which density fluctuations of order one occur. The second is the FDM analogue of the Jeans length. In linear perturbation theory, this is the length scale where the gravitational attraction balances the ‘quantum pressure’ resisting collapse, such that perturbations on larger scales grow, while smaller ones oscillate. Expressed as a wave number k_J , this is (Hu et al. 2000)

$$k_J = \left(\frac{6\Omega_m}{1+z} \right)^{1/4} \left(\frac{mH_0}{\hbar} \right)^{1/2} \quad (13)$$

as a function of the redshift z , with the Hubble parameter H_0 , and the cosmic matter density parameter Ω_m .

3 NUMERICAL METHODOLOGY

Our numerical simulations are performed using the same setup as in [May & Springel \(2021\)](#). We present two types of simulations: (1) FDM simulations using the `AXIREPO` code⁵ first introduced in [May & Springel \(2021\)](#), which is implemented as a module in `AREPO` ([Springel 2010](#)) and numerically solves the SP equations, eqs. (3) and (4), using a pseudo-spectral method, and (2) ‘standard’ N -body CDM simulations using the unmodified `AREPO` code, which implements the `TreePM` numerical method to solve the Vlasov–Poisson equations. For each type of simulation, we additionally compare and contrast two different kinds of ICs, corresponding to an FDM or CDM universe (see section 3.1).

As in our previous work, the simulation volume consists of a cubic box of side length L with periodic boundary conditions, sampling the matter distribution in the universe. The box is filled with dark matter (FDM or CDM) whose average comoving density is the cosmic mean background matter density

$$\langle \rho \rangle = \rho_m = \Omega_m \rho_{\text{crit}} = \Omega_m \frac{3H_0^2}{8\pi G}. \quad (14)$$

In the FDM case (pseudo-spectral SP solver), the fields ψ (‘wave function’) and Φ (‘potential’) are discretised on a uniform Cartesian grid with N^3 points, enabling the use of the Fast Fourier Transform (FFT). In the CDM case, as usual, the phase space of dark matter particles is sampled using (much) more massive ‘simulation particles’, whose trajectories are evolved using Newtonian gravitational dynamics.

Concerning FDM SP simulations, it is important to make note of the tremendous computational requirements involved. Firstly, for the pseudo-spectral method, ensuring the absence of ‘aliasing’ in the complex exponentials imposes a restriction on the size of the time step Δt ,

$$\Delta t < \min\left(\frac{4}{3\pi} \frac{m}{\hbar} a^2 \Delta x^2, 2\pi \frac{\hbar}{m} a \frac{1}{|\Phi_{\text{max}}|}\right), \quad (15)$$

where $\Delta x = L/N$ is the spatial grid resolution and Φ_{max} is the maximum value of the potential. Although the exact form of eq. (15) is specific to the pseudo-spectral method, the dependence $\Delta t \propto \Delta x^2$ seems to hold for all numerical approaches to the SP system of equations, eqs. (3) and (4), and serves as an illustration of the Schrödinger equation’s nature as a diffusion equation.

Secondly, a constraint on the validity of the spatial discretisation emerges from the relationship between the velocity field and the gradient of the wave function’s phase (eq. (10)), which implies that velocities v larger than a certain value v_{max} cannot be represented in a simulation with spatial resolution Δx :

$$v_{\text{max}} = \frac{\hbar}{m} \frac{\pi}{\Delta x}. \quad (16)$$

In other words, the ‘worst’ spatial resolution Δx_{max} that still yields acceptable results is (roughly) given by the de Broglie wave length corresponding to v_{max} :

$$\begin{aligned} \Delta x_{\text{max}} &= \frac{\pi \hbar}{m v_{\text{max}}} = \frac{1}{2} \lambda_{\text{dB}}(v_{\text{max}}) \\ \Leftrightarrow \Delta x &< \frac{\pi \hbar}{m v_{\text{max}}}. \end{aligned} \quad (17)$$

Or, rephrasing yet again, the de Broglie wavelength must be resolved for all velocities appearing in the simulation. As with the time step

⁵ The `AXIREPO` code will be made public in the near future (including the halo finder).

criterion, similar considerations mandate resolving the de Broglie wavelength also for other numerical methods for the SP equations, yielding a similar constraint.

Combined, the time step criterion (15), $\Delta t \propto \Delta x^2$, and the velocity criterion (17), $\Delta x \propto 1/v$, render simulations of large cosmological objects or representative cosmological volumes prohibitively expensive. Contrary to N -body simulations, the additional requirement on the spatial resolution makes it impossible to resort to coarser, low-resolution simulations while still obtaining valid results on all (large) scales that are still resolved. Instead, a lack of sufficient resolution will affect results even on the largest scales and within the linear regime of structure formation, as shown in [May & Springel \(2021\)](#).

Although numerical methods have been developed for FDM which are in principle more versatile or sophisticated, such as adaptive mesh refinement (AMR) or hybrid techniques ([Schwabe & Niemeyer 2022](#)), the unique computational demands of FDM have the effect that, except for specific cases where very high resolution is desired in a small region (‘zoom-in’), these methods still suffer from the tremendous cost involved in FDM simulations. While it may be argued that a uniform grid is wasteful in regions where a lower resolution would be sufficient, the velocity criterion (17) actually imposes significant demands on resolution even in low-density regions. The pseudo-spectral method used here, although not very flexible due to its limitation to a single uniform resolution, nevertheless has the advantage of unmatched accuracy in the spatial integration (at the given level of resolution), in addition to its use of a very simple and optimized algorithm in the form of the FFT, so it is at present one of the best ways to address the unique challenges of the SP system of equations.

3.1 Initial conditions

As in [May & Springel \(2021\)](#), the ICs were generated at the starting redshift $z = 1/a - 1 = 127$ using the `N-GENIC` code ([Springel 2015](#)), which employs the Zel’dovich approximation (or second-order Lagrangian perturbation theory) to generate a random realization of density fluctuations consistent with a prescribed power spectrum in terms of a perturbed, but otherwise regular particle distribution. We analyse and compare four different kinds of simulations (cf. section 3.2), differentiated by the solved dynamics (FDM/Schrödinger–Poisson and CDM/ N -body) and the initial power spectrum (‘standard’ Λ CDM and ‘self-consistent’ FDM ICs with a cut-off at small scales). For each case, a different approach for the ICs was necessary:

- CDM (N -body) dynamics: In this case, the particle distribution generated by `N-GENIC` can simply be used directly.
- FDM (Schrödinger–Poisson) dynamics: The initial wave function is constructed using the prescription

$$|\psi(\mathbf{x})| = \sqrt{\frac{\rho(\mathbf{x})}{m}}, \quad (18)$$

$$\nabla \arg(\psi(\mathbf{x})) = \nabla \theta(\mathbf{x}) = \frac{m}{\hbar} \mathbf{v}(\mathbf{x}), \quad (19)$$

where ρ is the matter density and \mathbf{v} the velocity (cf. eqs. (6) and (10); [Widrow & Kaiser 1993](#); [Mocz et al. 2018](#); [May & Springel 2021](#)). In this case, the random realization of the density fluctuation $\delta(\mathbf{x})$ in `N-GENIC` is actually used without creating a particle distribution at all, in order to avoid unnecessary transformation steps. For the absolute value of the complex wave function, the correspondence to the density via eq. (18) is straightforward. The wave function’s phase requires a few more steps, with the following result using eq. (19) (in Fourier space)

$$\mathcal{F}[\theta](\mathbf{k}) = -i \frac{m}{\hbar} \frac{\mathbf{k}}{k^2} \cdot \text{FFT}[\mathbf{v}](\mathbf{k}) \quad (20)$$

Type	IC	Res. el.	L / h^{-1} Mpc	mc^2 / eV	Resolution
FDM	FDM	8640 ³	10	7×10^{-23}	$1.16 h^{-1}$ kpc
FDM	FDM	6144 ³	10	5×10^{-23}	$1.63 h^{-1}$ kpc
FDM	FDM	4320 ³	10	3.5×10^{-23}	$2.31 h^{-1}$ kpc
FDM	FDM	4320 ³	10	2×10^{-23}	$2.31 h^{-1}$ kpc
FDM	FDM	4320 ³	10	1×10^{-23}	$2.31 h^{-1}$ kpc
FDM	CDM	8640 ³	10	7×10^{-23}	$1.16 h^{-1}$ kpc
FDM	CDM	4320 ³	10	3.5×10^{-23}	$2.31 h^{-1}$ kpc
CDM	FDM	2048 ³	10	7×10^{-23}	$9.69 \times 10^3 h^{-1} M_\odot$
CDM	FDM	2048 ³	10	3.5×10^{-23}	$9.69 \times 10^3 h^{-1} M_\odot$
CDM	CDM	2048 ³	10	—	$9.69 \times 10^3 h^{-1} M_\odot$

Table 1. List of performed simulations with important characteristics: simulation type (FDM/SP or CDM/ N -body), number of resolution elements (grid cells or N -body particles), box size, FDM particle mass, and resolution (grid cell size or N -body particle mass). The lengths given for the box sizes and resolutions are comoving. The simulations with CDM ICs have previously been presented in [May & Springel \(2021\)](#).

where \mathbf{v} is the velocity field in the Zel’dovich approximation.

- **CDM initial power spectrum:** The simulations for this case are the ones previously presented in [May & Springel \(2021\)](#). The ICs were generated with an input power spectrum following [Efstathiou et al. \(1990, 1992\)](#), i. e. of the form

$$P_{\text{CDM}}(k) \propto k \left[1 + \left(ak + (bk)^{\frac{3}{2}} + c^2 k^2 \right)^\nu \right]^{-\frac{2}{\nu}}, \quad (21)$$

with $a = 6.4/\Gamma h^{-1}$ Mpc, $b = 3.0/\Gamma h^{-1}$ Mpc, $c = 1.7/\Gamma h^{-1}$ Mpc, $\Gamma = \Omega_m h = 0.21$,⁶ and $\nu = 1.13$. Here $h = H_0/(100 \text{ km s}^{-1} \text{ Mpc}^{-1})$ encodes the Hubble constant.

- **FDM initial power spectrum:** In this case, we make use of the power spectrum predicted in linear theory by the code `AXIONCAMB` ([Hlozek et al. 2015](#); [Grin et al. 2022](#)) for an axion cosmology. However, in order to be able to compare our simulations as directly as possible, we aim to minimize differences in the CDM and FDM ICs arising from the two different methods (a fitting function eq. (21) and a numerical Boltzmann code). To this end, instead of using the power spectrum $P_{\text{AXIONCAMB,FDM}}(k)$ from `AXIONCAMB` directly, we also calculated the corresponding Λ CDM power spectrum $P_{\text{AXIONCAMB,CDM}}(k)$ using the same code and obtained the final input spectrum $P_{\text{FDM}}(k)$ as follows:

$$P_{\text{FDM}}(k) = \frac{P_{\text{AXIONCAMB,FDM}}(k)}{P_{\text{AXIONCAMB,CDM}}(k)} P_{\text{CDM}}(k). \quad (22)$$

This ensures that any variations between eq. (21) and `AXIONCAMB` are cancelled out, and only the differences arising from the choice of the CDM or FDM model remain.

3.2 Simulations

The simulations were performed using the cosmological parameters $\Omega_m = 0.3$, $\Omega_b = 0$, $\Omega_\Lambda = 0.7$, $H_0 = 70 \text{ km s}^{-1} \text{ Mpc}^{-1}$ ($h = 0.7$), and $\sigma_8 = 0.9$,⁷ with ICs as described in section 3.1. The same cosmological parameters and random seeds were shared for the generation of all ICs at $z = 127$ in order to allow for a direct comparison between different dark matter models and resolutions, including those previously presented in [May & Springel \(2021\)](#). For a comoving box size of $10 h^{-1}$ Mpc, and different masses m , simulations

with different resolutions – up to grid sizes of $N^3 = 8640^3$ – were performed. As before, the simulations were run until $z = 3$, where the FDM simulations should still be largely unaffected by resolution effects. Furthermore, even the largest modes in simulations of this box size would become non-linear before $z = 0$, making the reliability and benefit of evolving simulations to this point dubious in any case. A detailed list of the different simulations is given in Table 1. A visual overview showing the projected density across a slab of the simulation volume is displayed for a subset of the simulations in Fig. 1. The images readily make differences between the four different kinds of simulations we have carried out apparent, and they show the impact of different values of m as well.

Most of the simulations listed in Table 1 focus on the mass values $mc^2 = 3.5 \times 10^{-23}$ eV and 7×10^{-23} eV, respectively, used in [May & Springel \(2021\)](#), but we also performed additional ‘self-consistent’ FDM simulations (SP + FDM ICs) for $mc^2 = 1 \times 10^{-23}$ eV, 2×10^{-23} eV and 5×10^{-23} eV in order to investigate the dependence of FDM phenomenology on the particle mass. For the lighter masses 1×10^{-23} , and 2×10^{-23} , the resolution (with respect to eq. (17)) is actually much better than that of the other simulations, allowing us to evolve them further in time beyond $z = 3$ (although once again with the caveat that all spatial modes eventually become non-linear). For N -body simulations, a very high mass resolution (large number of particles) was used when compared to most similar cosmological simulations. This was done in order to be able to measure the power spectrum down to very small scales, comparable to those accessible using a 8640³ grid. Due to our earlier work in [May & Springel \(2021\)](#) using the same parameters, it was not necessary to investigate the numerical convergence of the simulations again in detail.

Although progress has been made e. g. in hybrid methods ([Schwabe & Niemeyer 2022](#)), which do not solve the equations of motion for the full wave dynamics everywhere, our simulations remain the largest cosmological SP simulations of structure formation with FDM. The new simulations with FDM ICs allow us to perform a four-way comparison between SP and N -body dynamics on the one hand, and FDM and CDM ICs on the other hand, and to quantify the impact of both aspects. Apart from being able to study a self-consistent FDM cosmology, this also allows us to gain insight into the extent to which FDM can be approximated (e. g.) by using N -body simulations with a modified initial power spectrum, and to examine the validity of previous work which took this approach (e. g. [Schive et al. 2016](#)).

3.3 Halo identification with suppressed small-scale power

In order to identify dark matter haloes, the friends-of-friends (FoF)-like halo finder developed in [May & Springel \(2021\)](#), which is able to work on a Cartesian grid, was used. Instead of a linking length for particle distances, this grid-based halo finder uses a density threshold as an analogous parameter. Only grid cells above the given overdensity threshold are considered, and they are always linked if they are adjacent.

While this approach worked very well for SP simulations with CDM-like ICs and an overdensity threshold of $60\rho_m$, the results with FDM ICs were very different. In this case, haloes are linked via *continuous, smooth, dense filaments* throughout the entire simulation volume. The central densities of these filaments exceed the threshold value of $60\rho_m$, leading to much larger regions of space being linked by the halo finder than intended. Indeed, as illustrated in Fig. 2, the largest FoF group traces a network of filaments and spreads across the entire simulation box, incorporating numerous haloes and filaments. This has dire consequences for the endeavour of actually identifying

⁶ See section 3.2.

⁷ As usual, the density parameters Ω_i indicate the values at $z = 0$.

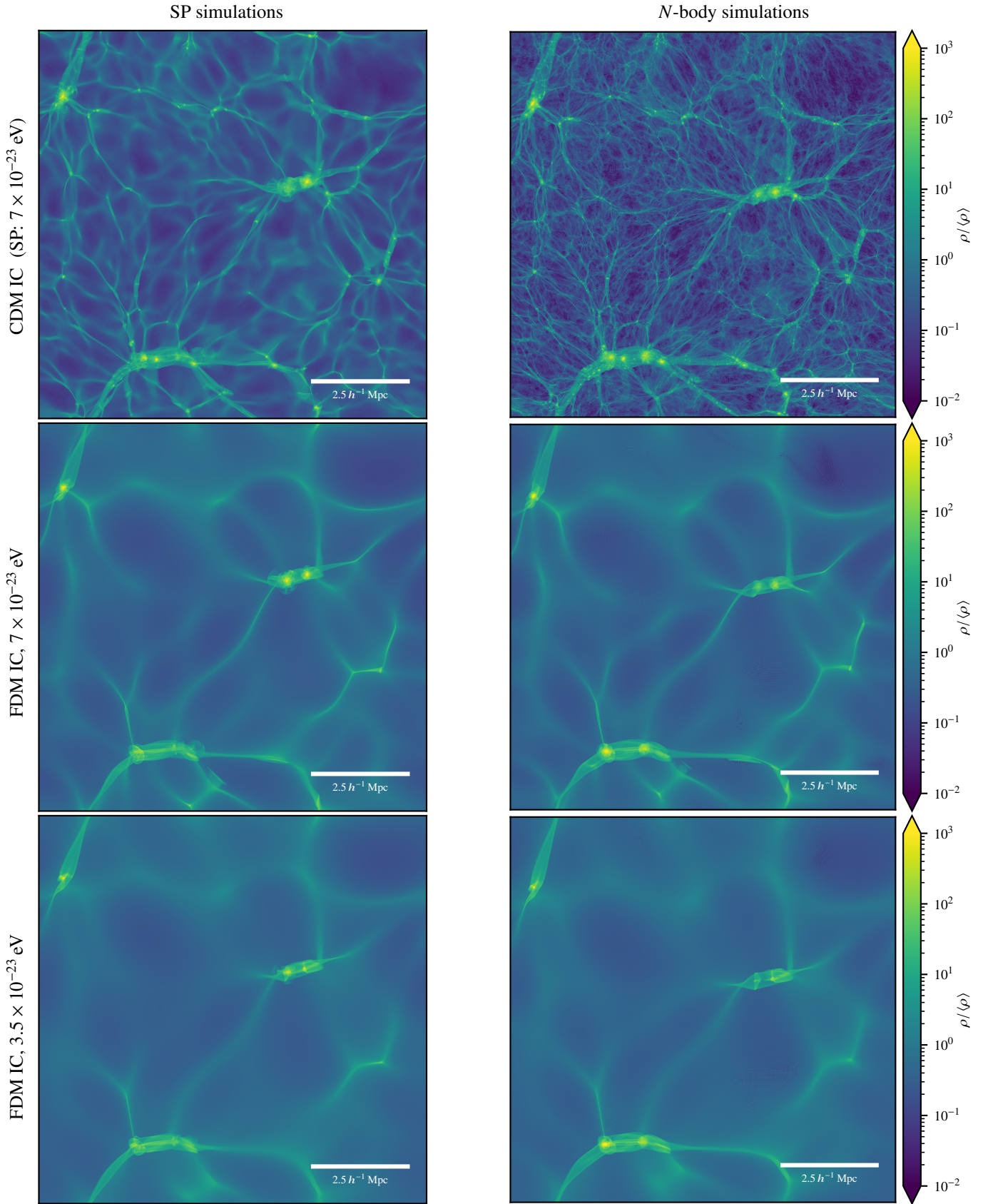


Figure 1. Projected dark matter densities along a thin ($100 h^{-1}$ kpc) slice in cosmological box simulations for different dynamics (FDM/SP, left column; or CDM/ N -body, right column) and ICs (FDM or CDM, rows), for box sizes $L = 10 h^{-1}$ Mpc at $z = 3$.

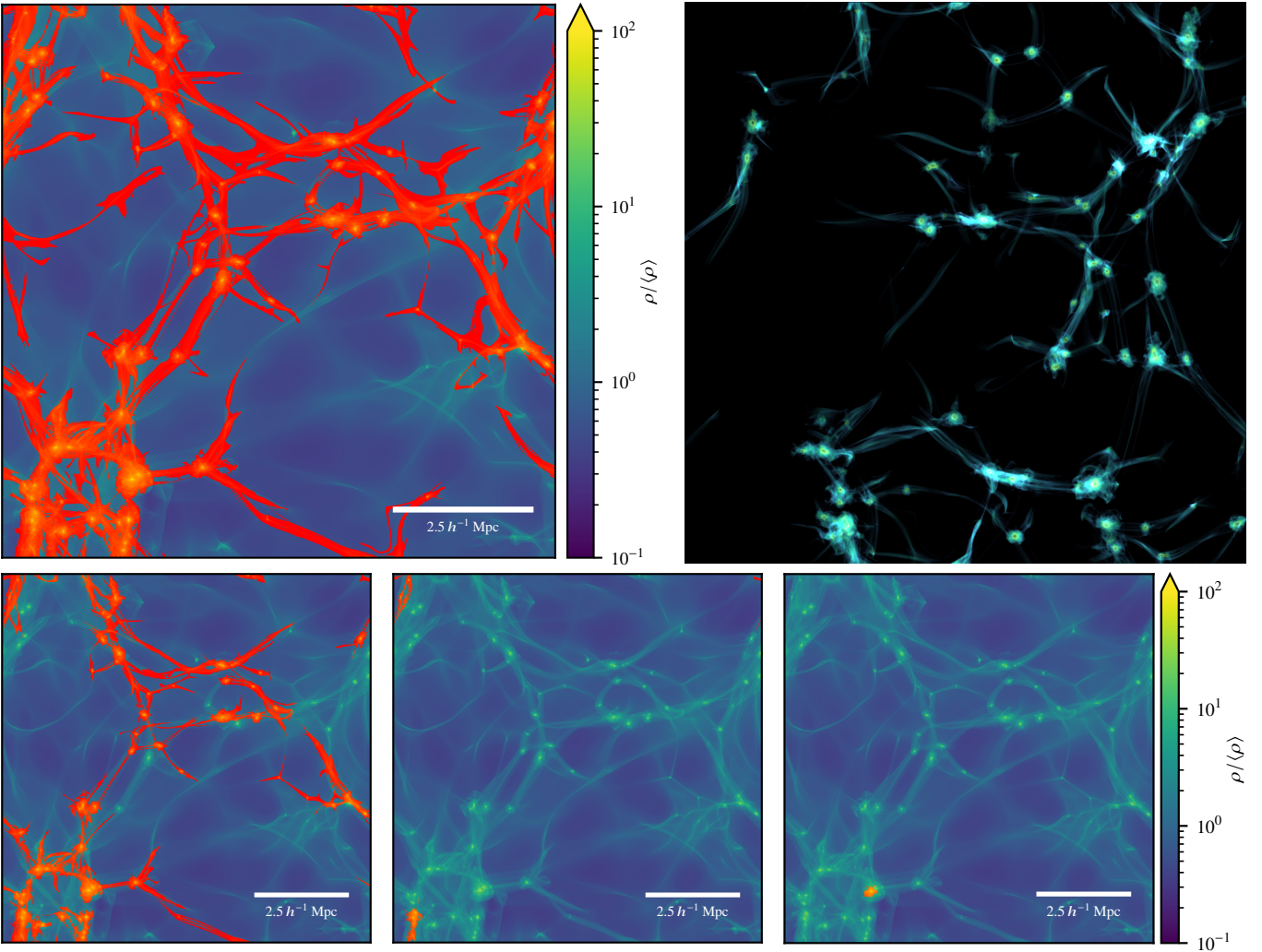


Figure 2. Projected dark matter density and volume rendering (different viewing angle) showing the largest FoF group using a halo finder overdensity threshold of $60\rho_m$ (top row), and $100\rho_m$, $200\rho_m$ and $300\rho_m$ (bottom row) in a cosmological box simulation of FDM at $z = 3$ with box size $L = 10 h^{-1}$ Mpc, grid size $N^3 = 8640^3$, FDM mass $mc^2 = 7 \times 10^{-23}$ eV, and FDM ICs. The areas marked in red/orange in the projections and shown in the volume rendering indicate regions spanned by the largest FoF group identified by the halo finder using the given overdensity threshold.

individual haloes: Because each FoF group is counted at most as a single halo, the largest group subsumes many haloes and thus leads to a severe under-counting. As shown in Fig. 3, the resulting HMF shows very few or even no haloes at all across wide mass ranges.

In order to break the filamentary links between haloes, it was necessary to use a higher value for the overdensity threshold. Although the FoF groups are smaller as a consequence, encompassing only the denser inner parts of haloes, this removes the filaments, which do not typically reach such high densities, from the groups. Empirically, we arrived at using a value of $300\rho_m$ to reliably prevent spurious connections between and merging of FoF groups (cf. Fig. 3).

However, this countermeasure invokes another problematic effect: Now, FoF groups are broken up into many small parts which do not all correspond to actual and reasonably complete haloes. Fig. 3 shows how increasing the group finder’s threshold leads to an ever larger proliferation of low-mass objects in the HMF. Clearly, these objects are spurious artefacts, since, as visible in Fig. 3, their number keeps increasing with the threshold parameter, eventually even exceeding the CDM IC case, which can be viewed as an upper limit for the HMF expected for FDM ICs.

On visual inspection of a sample of these objects, it turned out that the vast majority of them are localized density fluctuations arising from the wave nature of FDM, e. g. in the form of constructive interference fringes, which can reach very high densities. The top panel of Fig. 4 shows how a large number of transient interference maxima is erroneously identified as haloes. Although the same patterns are present in the FDM simulations with CDM ICs, the lower threshold value of $60\rho_m$ ensured that these objects remained connected to haloes within a single FoF group.

In the end, filtering this set of FoF groups using a gravitational binding criterion proved necessary and successful for reliably identifying haloes. To this end, we compute the ‘self-potential’ of each FoF group within R_{200} , i. e. the gravitational potential V_s generated only

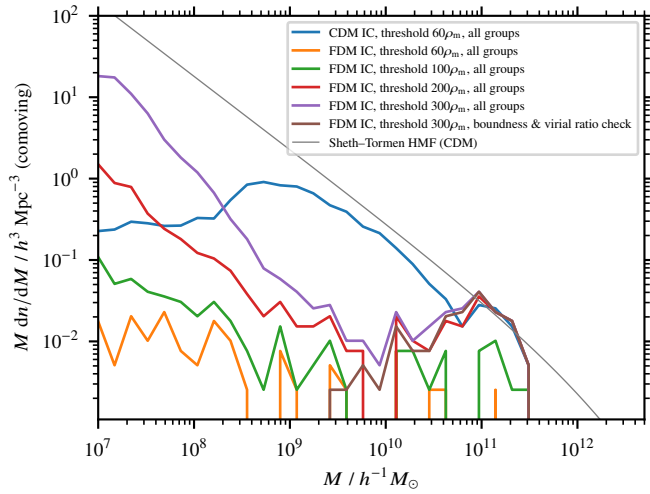


Figure 3. Halo mass function of a cosmological FDM simulations at $z = 3$ with a box size of $L = 10 h^{-1}$ Mpc and FDM ICs for different values of the halo finder’s overdensity threshold and after filtering using the gravitational binding criterion. Different simulations are shown as labelled.

by the matter within R_{200} ,⁸

$$V_s = -\frac{1}{2} \sum_{\substack{i,j \\ i \neq j}}^{|r_i - r_j| < R_{200}} \frac{G m_i m_j}{|r_i - r_j|}, \quad (23)$$

as well as the kinetic energy T_v in the group’s center-of-mass frame using eq. (8) and the gradient energy T_ρ , and excluded any FoF group which did not meet the binding criterion

$$E = T_v + T_\rho + V_s < 0, \quad (24)$$

cf. eq. (11). This reliably excludes the gravitationally unbound, transient wave interference patterns.

It should be noted that the computation of velocities from the complex wave amplitude ψ using the gradient of the phase as in eq. (10) is not straightforward. Not only is it the phase a periodic variable, making it necessary to take into account wrap-arounds at 2π when computing gradients, but it is also undefined in regions of destructive interference, where $\rho \rightarrow 0$. In the end, we found the most robust method to be using the (equivalent) definition via the momentum density in eq. (8). Not only does this avoid the treatment of the periodic phase variable, but it is also well-defined even for $\rho = 0$, preventing pathological cases (extremely large velocities) when computing the numerical derivative. Although obtaining the velocity from the momentum density requires dividing by ρ , the results of this procedure turn out to be much more well-behaved in practice.

Finally, in addition to the above, we enforced a stricter cut on the virial ratio $-2T/V$ in the form of

$$-2T/V_s < 1.6 \quad (25)$$

in order to eliminate a number of objects which were clearly highly perturbed objects and not reasonably relaxed haloes.⁹ Similar cuts are regularly applied in CDM models when density profiles of haloes

⁸ The self-potential calculation was here done using direct summation, approximating each grid cell as a point particle for simplicity, which is accurate up to hexadecupole order in the multipole expansion (Barnes & Hut 1989).

⁹ Since eq. (24) corresponds to $-2T/V_s < 2$, eq. (25) automatically enforces gravitational binding as well.

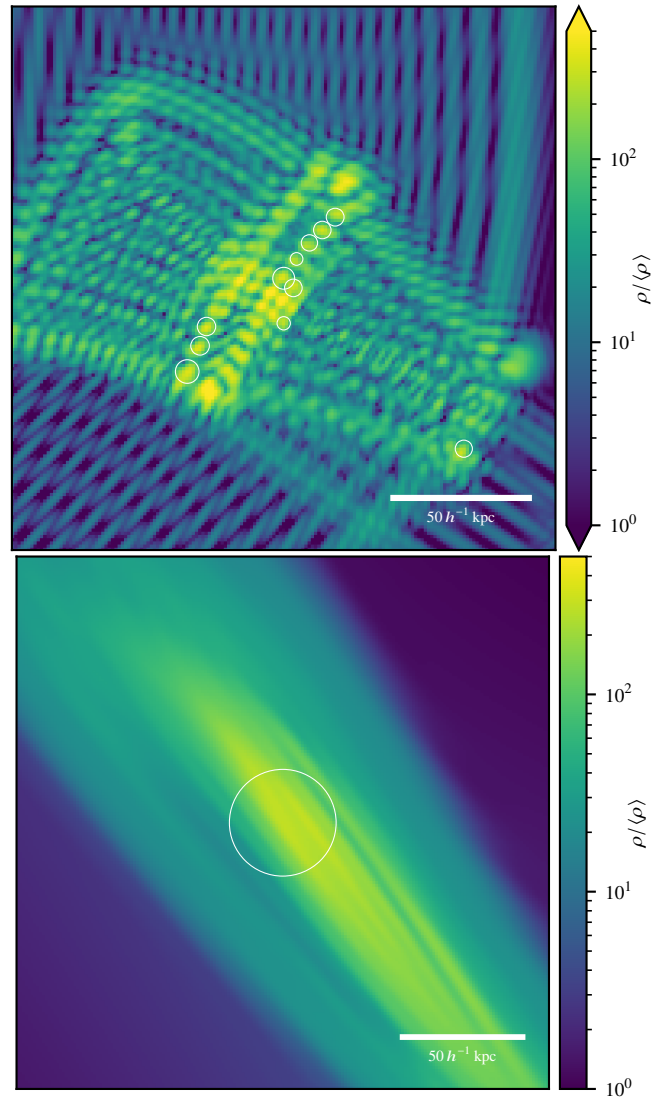


Figure 4. Examples of spurious FoF groups identified in FDM interference patterns (top) and filaments (bottom) in a cosmological FDM simulation (projected density). The former arise in great numbers as a consequence of raising the halo finder’s overdensity threshold to $300\rho_m$, while the latter appear due to a lack of small-scale power analogous to WDM. The circles mark the groups’ locations, with the radius corresponding to R_{200} .

are studied (e. g. Neto et al. 2007). These objects are distinct from the wave interference phenomena, and instead could be called very high-density filamentary structures, arising from the lack of power on small scales in the FDM ICs case. Their high virial ratios indicate that, while gravitationally bound, they have not reached a virialised state. In contrast, for CDM, such filaments do not remain smooth, but fragment into (sub-)haloes down to the smallest scales. Examples of both kinds of non-halo objects are shown in Fig. 4.

Fig. 5 shows the virial ratios for FoF groups in an FDM simulation as a function of M_{200} (determined using a spherical overdensity algorithm). Although a virial ratio of ≈ 1 , corresponding to $2T \approx |V|$, would be expected for virialised objects, there is a significant bias of many objects around $-2T/V_s \approx 1.2$. Indeed, this effect has been observed for CDM haloes in N -body simulations as well (Bett et al. 2007; Neto et al. 2007), and seems to be due to the definition of the self-potential, which neglects the contribution from a possible

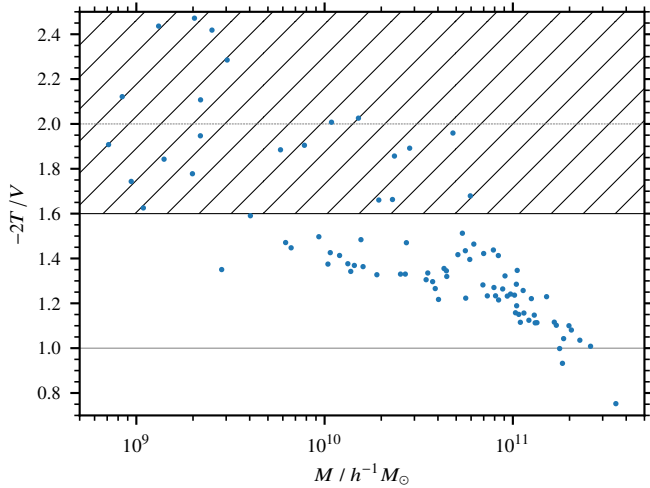


Figure 5. Virial ratios $-2T/V$ for FoF groups identified by AxIREPO’s halo finder with an overdensity threshold of $300\rho_m$ in a cosmological FDM simulation at $z = 3$ with $L = 10 h^{-1} \text{ Mpc}$, $N^3 = 8640^3$, $mc^2 = 7 \times 10^{-23} \text{ eV}$ and FDM ICs. The potential energy V is the ‘self-potential’, and both T and V are summed within a radius of R_{200} for each halo. Points above the dashed line correspond to FoF groups which are not gravitationally bound ($E = T + V > 0$). Points in the hatched region ($-2T/V > 1.6$) are excluded from our definition of ‘haloes’.

large-scale tidal field (Stücker et al. 2021). A more sophisticated approach, such as the ‘boosted potential binding check’ from Stücker et al. (2021), can potentially improve the results, but was not necessary in our case, perhaps due to the low number of remaining haloes after selection, which allows for easy manual inspection of the end result. Notably, these problems of (1) enormous FoF groups, linked by smooth filaments, stretching across 10s of Mpc, and (2) additional, non-virialised structures identified by the halo finder, have been encountered in N -body simulations of WDM before (Angulo et al. 2013; Stücker et al. 2021, esp. figs. 2 and 4). There have also been speculations that stars themselves may form in WDM filaments (Gao & Theuns 2007), giving rise to a qualitatively different mode of galaxy formation compared to CDM.

4 FOUR-WAY COMPARISON OF THE POWER SPECTRUM

The matter power spectrum is a crucial measure of matter clustering at different length scales. For Λ CDM, even including baryonic effects, its behaviour and temporal evolution have been determined rather accurately using numerical simulations (e. g. Jenkins et al. 1998; Hellwing et al. 2016; Springel et al. 2018). For FDM, linear structure formation is scale-dependent even in linear perturbation theory, with a suppression at scales smaller than the FDM Jeans length $\lambda_J = 2\pi/k_J$ (13), and even during non-linear evolution on scales where the wave nature of FDM is relevant, i. e. at or below the de Broglie wavelength λ_{dB} (12). Intuitively, this can be understood as a consequence of the analogue of the Heisenberg uncertainty principle (Schrödinger formulation), or, equivalently, the presence of the so-called ‘quantum pressure’ (Madelung fluid formulation).

Combined with our previous results (May & Springel 2021), our new simulations with FDM ICs, using both SP and N -body solvers, allow us to draw a four-way comparison of observables, contrasting results for each combination of ICs (FDM vs. CDM) and dynamics (SP/‘FDM’ vs. N -body/‘CDM’). Although only two of the four cases are strictly self-consistent in a physical sense (namely, FDM and CDM

with their corresponding ICs), this approach allows us to disentangle the two essential physical differences distinguishing FDM from CDM in cosmological numerical simulations: the initial conditions and the dynamics on small scales. This is particularly relevant to evaluate to what extent approximate methods, such as the use of N -body simulations with an FDM initial power spectrum (Schive et al. 2016; Mocz et al. 2020), can yield reasonable results.

In Fig. 6, we show the measured matter power spectra for both FDM and CDM cases, where simulations with $mc^2 = 7 \times 10^{-23} \text{ eV}$ are used to represent FDM. The solid lines (CDM ICs) correspond to the results from May & Springel (2021), whereas the dashed lines are the new simulations with FDM ICs added in this work. Reassuringly, all cases accurately agree with each other and with linear perturbation theory on large scales and at early times, and it can be observed again that the onset of non-linear structure formation is delayed for FDM, and does not proceed strictly in the same bottom-up fashion as for CDM.

As a reflection of this fact, the differences between the four cases exhibit variations across time. For example, only the N -body CDM simulation significantly exceeds linear growth at redshifts below 15, although the SP CDM case has similar, mild non-linear amplification on large enough scales of $k \approx 10 h \text{ Mpc}^{-1}$ to $20 h \text{ Mpc}^{-1}$ at $z = 15$. However, by $z = 7$, considerable non-linear enhancement is present on small scales $k \gtrsim 5 h \text{ Mpc}^{-1}$ in all cases.

Indeed, for $z \geq 7$, the power spectra for simulations with the same ICs track each other comparatively closely on all scales, although the SP simulations are still suppressed by some tens of percent for $k \gtrsim 10 h \text{ Mpc}^{-1}$. There seems to be little qualitative change in the relative evolutions of the power spectra beyond $z = 7$. Notably, for the most part during this time, the difference between SP and N -body is significantly smaller than that between the different sets of ICs, and is of similar size in both cases.

At $z = 3$, SP and N -body results drift more apart compared to earlier times ($z = 7$, $z = 5$). Interestingly, at this time, the relative difference between the dynamics and the ICs is now roughly the same, meaning that each of the two physical ‘ingredients’ has a similar impact at this time. Since the time evolution stops at $z = 3$, it is however unclear whether this is the onset of a new, sustained phenomenological difference or whether it is a transient, numerical artefact. Since the resolution requirements for SP grow more stringent towards later times, it is also possible that these slight relative changes in the power spectra are the first hints of resolution effects affecting the results.

An interesting difference for the SP simulations with different ICs is the location of the ‘bump’ on small scales, which starts to appear at $z = 7$. At the location of this bump, the small-scale power in SP simulations matches or even slightly exceeds the CDM power (for FDM ICs, the SP simulation quite significantly surpasses its N -body companion on these scales). It is commonly attributed to the presence of FDM interference patterns and granules of size λ_{dB} (Mocz et al. 2020), which are unique to the wave nature of FDM and not present in CDM. However, curiously, there is a shift in the location of this bump for the two SP simulations, with the bump in the FDM IC case appearing on smaller scales. Following the interpretation that the bump is linked to λ_{dB} , this would imply that the FDM simulation displays more power on smaller wavelengths, which (with the other parameters being equal) would correspond to higher velocities. The physical origin of this effect remains unclear and is a subject for future investigation.

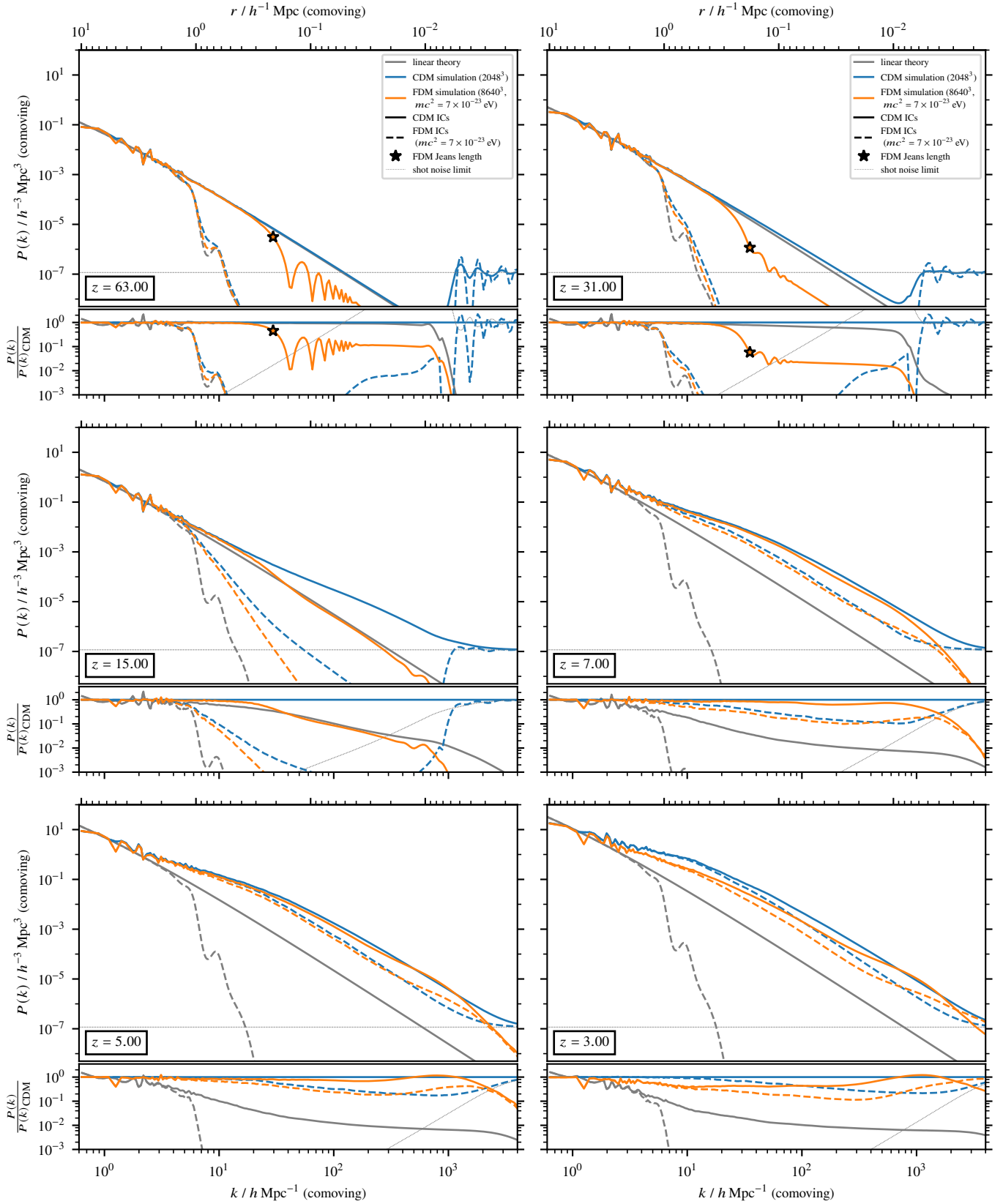


Figure 6. Four-way comparison of dark matter power spectra at different redshifts for cosmological FDM (wave) and CDM (N -body) simulations with FDM and CDM ICs in $L = 10 h^{-1} \text{ Mpc}$ boxes. The power spectrum evolved using linear perturbation theory is shown for comparison. The lower panels show the ratio of the power spectra to the CDM result (N -body simulation with CDM ICs). For $z = 63$, the dashed line additionally indicates the FDM Jeans scale (eq. (13)). Faint dotted lines show the shot noise limits of the N -body simulations; the power spectrum cannot be measured accurately once this limit is reached.

5 THE HALO MASS FUNCTION

The formation of gravitationally collapsed structures of dark matter, so-called haloes, is one of the most significant results of cosmic structure. In particular, haloes serve as the loci of collapse of baryonic matter and thus provide the environment for the formation and evolution of galaxies. The HMF, which is a measure of halo abundance as a function of mass, and its evolution across time, are thus critical benchmarks of a cosmological model.

While the (extended) Press–Schechter formalism (Press & Schechter 1974; Sheth & Tormen 1999) has been demonstrated to be a simple and reliable method to estimate the HMF and its evolution (depending only on the power spectrum and growth factor in *linear* perturbation theory), with its validity being confirmed by comparisons to non-linear N -body simulations (which has also allowed for the calibration of more accurate empirical fits, e.g. Jenkins et al. 2001; Tinker et al. 2008; Despali et al. 2016), there is no similar, simple approximation for FDM. None of the few existing (semi-)analytic estimates, such as using a Jeans-filtered power spectrum to account for the effects of ‘quantum pressure’ (Marsh & Silk 2014; Du et al. 2017), or a sharp k -space filtering in the Press–Schechter formalism with a variable cut-off (Kulkarni & Ostriker 2022), have been verified using the full non-linear SP evolution, rendering their quantitative reliability still unclear. The closest substitution of this goal thus far has been reached by comparing to the FDM HMF estimate in Schive et al. (2016), which employed the approximate technique of collisionless N -body simulations with truncated initial fluctuation spectrum (but *without* the full SP dynamics), similar to those we have performed in this work as well (“CDM with FDM ICs”). This type of simulation technique is also how WDM models are often computed (e.g. Lovell et al. 2014), but importantly it exhibits a number of by now well-known difficulties (Wang & White 2007), such as the creation of ‘spurious’ low-mass haloes that necessitate special removal procedures and ultimately introduce a significant source of uncertainty.

Supplementing our previous results (May & Springel 2021), our new simulations allow for a measurement of the HMF in a fully self-consistent cosmological wave simulation of FDM for the first time. For this purpose, we made use of the FoF-based grid halo finder in AXI-REPO to identify collapsed structures in our SP simulations. However, as discussed in section 3.3, the cut-off in the FDM initial power spectrum actually introduces considerable complications in identifying bound structures – some of which similarly plague WDM simulations (Wang & White 2007; Angulo et al. 2013) –, which mandate the application of additional filtering steps on the initial group catalogue determined by the halo finder. When implementing them, it turns out that only a limited number of most massive haloes in the raw catalogue survive in our FDM simulation and can be considered physically robust, bound structures. Projections of these 68 haloes at $z = 3$ are displayed in Fig. 7, making it clear that the majority of them exhibit a morphology in their outer parts that is quite distinct from what is typically seen in CDM simulations. In particular, the haloes are usually embedded in thick filaments that show clear patterns of interference ridges.

In Fig. 8 we show the resulting HMF for the new FDM simulations compared to the mass functions for CDM ICs. The results for the HMF make it clear that the ICs have a much stronger impact than the choice of SP or N -body dynamics. Due to the cut-off on small scales in the initial FDM power spectrum, the seeds of structure formation are suppressed, and it becomes virtually impossible for haloes below a certain mass threshold to form. While the SP dynamics also implies a threshold for the formation of virialised objects, this is drastically

raised when introducing FDM ICs. Indeed, this behaviour is illustrated quite starkly by the fact that there are only 68 bound haloes in our entire simulation volume at $z = 3$, whereas the SP simulation with CDM ICs contains thousands of haloes in the same (quite moderate) volume at the same time.

Although the statistics are somewhat poor due to the small number of resulting simulated haloes – despite our efforts to simulate a larger volume than has been standard for SP simulations thus far – we can measure the HMF with reasonable accuracy and arrive at an important result: There appears to be quite good agreement between the HMF measured in our fully self-consistent FDM wave simulation and the fitting function of Schive et al. (2016), which was determined from N -body simulations with an FDM power spectrum. Consistent with our conclusion above, this confirms that the ICs are the primary factor in determining the FDM HMF, and that the use of N -body simulations with filtering techniques is in principle sufficient to obtain at least an approximate estimate of the HMF in an FDM cosmology.

The (semi-)analytic estimates obtained in Du et al. (2017); Kulkarni & Ostriker (2022), on the other hand, differ from the result obtained using this technique: Both feature a steeper turnover and drop at low masses than measured in simulations, and while the former results in a similar cut-off mass, it underestimates the number of haloes for high masses and overestimates it for low masses near the cut-off, whereas the latter features a lower cut-off mass, which does not account for the presence of the lower-mass haloes we find here. Thus, compared to methods based on the extended Press–Schechter formalism, the N -body approximation seems to be the most reliable ‘simplified’ approach to the HMF so far, as it yields the best match to our measurements in full FDM simulations.

Unfortunately, given the small number of haloes present even at our final redshift $z = 3$, it is not possible for us to meaningfully study the evolution of the HMF with redshift in our simulation volume and to explicitly confirm that this conclusion also holds at other redshifts. Likewise, reliably characterising the quantitative precision of fitting functions such as those of Schive et al. (2016) will have to await FDM simulations with much larger volumes and hence better statistics.

6 FUZZY DARK MATTER FILAMENTS

Our findings concerning the stark departure of the nature of filaments in FDM compared to CDM in section 3.3, and in particular their different visual appearance of the outer parts of haloes, compelled us to further investigate FDM filaments. In Fig. 2, we provide an image of the cosmic web in FDM, which is quite unlike the more familiar structures expected for CDM, and is thus adding to this motivation. Previous results for WDM and smaller ‘proof-of-concept’ simulations of FDM have already provided hints that filaments represent another, second type of significant object when it comes to baryonic processes such as star formation (e.g. Gao & Theuns 2007; Gao et al. 2015; Mocz et al. 2020). Contrary to CDM, where filamentary structures fragment into (sub-)haloes down to the smallest scales, the filaments in these models stay intact as smooth, overdense, large-scale dark matter structures.

We have used the DISPERSE code (Sousbie 2011; Sousbie et al. 2011) in order to attempt to identify the filaments in our FDM simulations. Unfortunately, this approach was met with technical difficulty due to computational limitations of the DISPERSE software. In particular, the code can only operate on shared-memory architectures, with no capabilities for today’s distributed-memory parallel computing infrastructure using the Message Passing Interface (MPI) standard. This means that it is inherently limited to the amount of memory

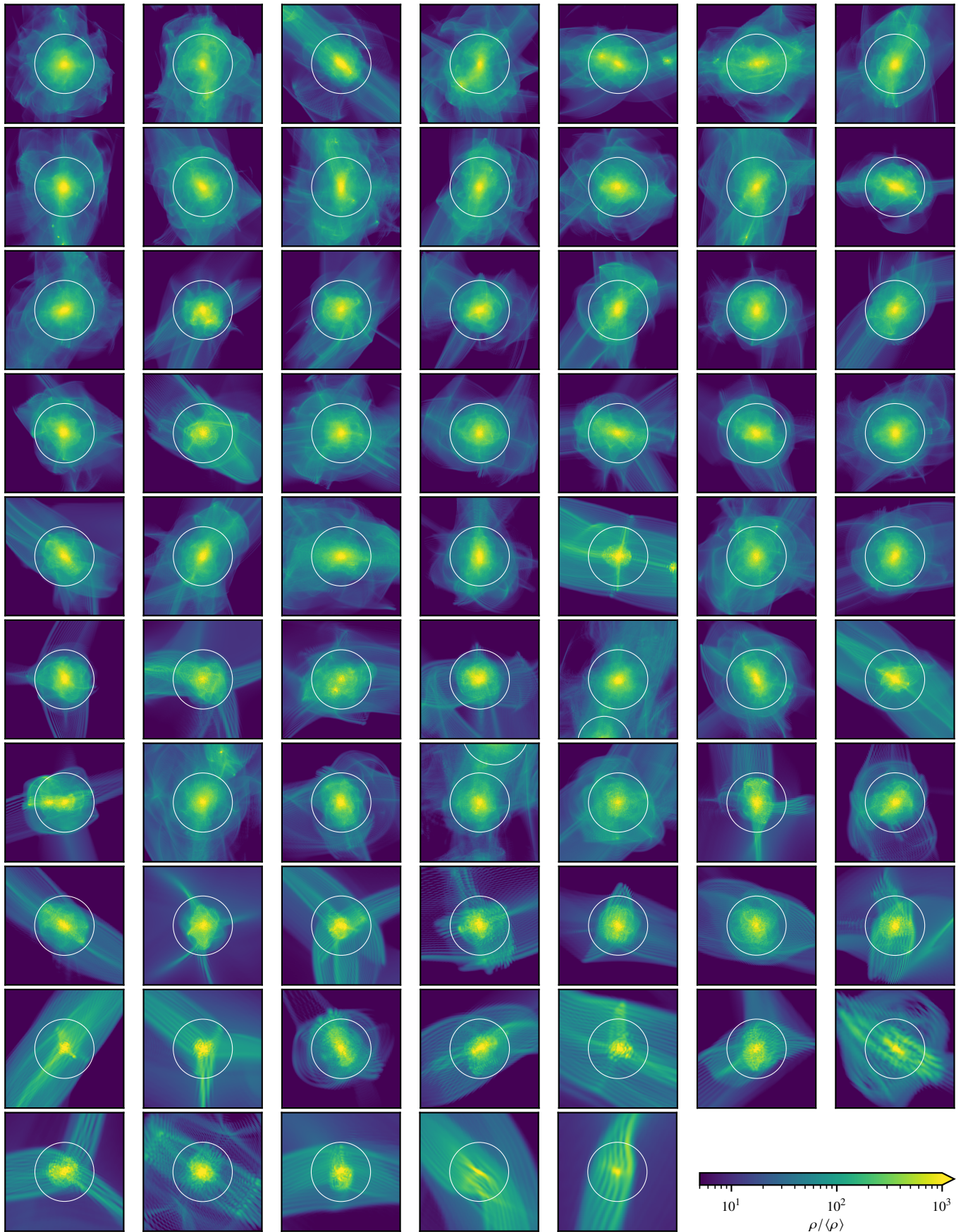


Figure 7. Projected dark matter densities for all 68 identified haloes at $z = 3$ in a cosmological FDM simulation with box size $L = 10 h^{-1}$ Mpc, grid size $N^3 = 8640^3$, FDM mass $mc^2 = 7 \times 10^{-23}$ eV, and FDM ICs. The projection depth is $2R_{200}$ for each halo.

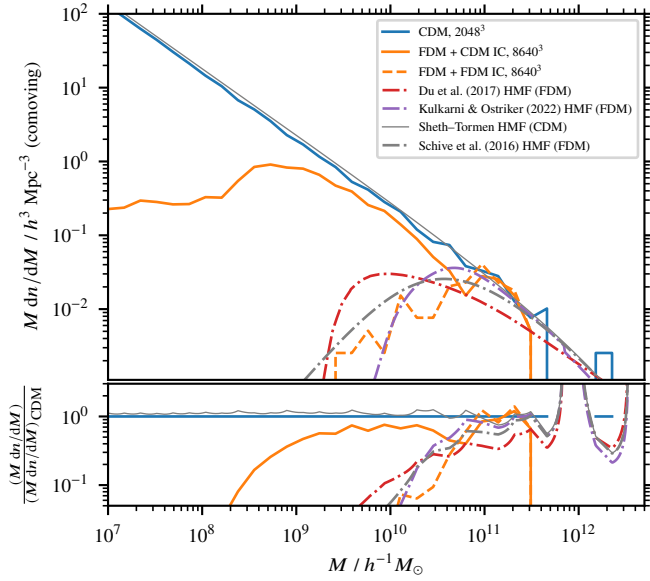


Figure 8. Halo mass functions of cosmological FDM and CDM simulations at $z = 3$ with FDM mass $mc^2 = 7 \times 10^{-23}$ eV, a box size of $L = 10 h^{-1}$ Mpc and different ICs. The HMF derived for CDM by [Sheth & Tormen \(1999\)](#) is shown for comparison. Different predictions for the FDM HMF from [Schive et al. \(2016\)](#); [Du et al. \(2017\)](#); [Kulkarni & Ostriker \(2022\)](#) are shown using dash-dotted lines. The lower panel shows the ratios of the mass functions to the result of the CDM simulation.

present on a single node on a computing cluster. Gravely exacerbating the problem is the fact that the `DISPERSE` algorithms are rather memory-intensive. Even with the largest amount of memory available to us on the Max Planck Computing and Data Facility (MPCDF)’s Raven system, which amounts to two terabytes, we were forced to severely ‘down-sample’ our simulated density fields in order to allow them to be processed by `DISPERSE`. We note that previous work applying `DISPERSE` to find filaments in large cosmological simulations, such as [Galárraga-Espinosa et al. \(2020\)](#), were able to avoid this problem by applying the code on a tracer field only, such as the distribution of galaxies. However, this option is not available in our case, because there are no objects (such as haloes) present in the dark matter filaments which could serve as a tracer field with appropriate sampling rate. Rather we need to identify filaments directly in the smooth dark matter density field.

In order to ensure comparability between SP (FDM) and N -body (CDM) simulations, we have constructed a CDM density field by binning the N -body particles to a Cartesian grid using cloud-in-cell (CiC) mass assignment, making the input to `DISPERSE` a uniform Cartesian grid of the density field in both cases. For FDM, the original 8640^3 grid was smoothed and scaled down by computing the means of neighbouring cells. A cut value of $60\rho_m$ was used, which is the minimum threshold difference between critical points in order for `DISPERSE` to keep them. This ensures that the identified structural complex is not swamped by tiny small-scale fluctuations in the density field.

In the end, the largest grids which we could process with `DISPERSE` were of size 288^3 for our largest FDM simulation, and 260^3 for its CDM counterpart. This of course drastically reduces the spatial resolution (to $34.7 h^{-1}$ kpc and $38.5 h^{-1}$ kpc, respectively), and thus cannot be expected to yield either the full population of simulated filaments or their precise locations. However, it nevertheless results

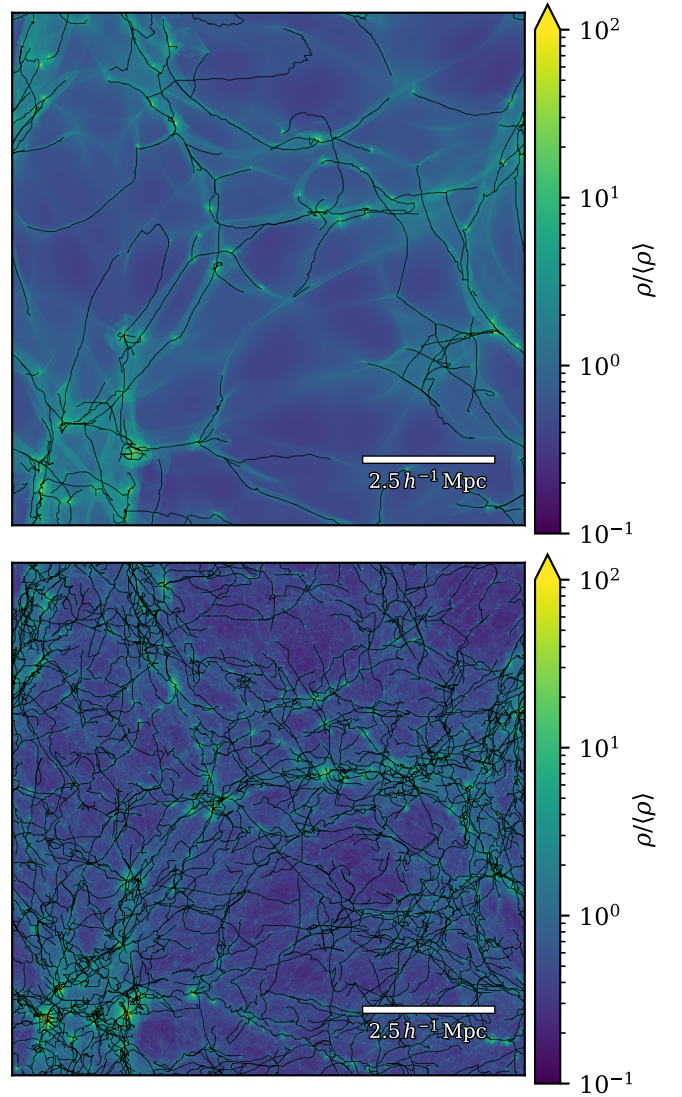


Figure 9. Projected dark matter density showing the filaments identified by `DISPERSE` (marked using black lines) in a cosmological box simulation of FDM at $z = 3$ with box size $L = 10 h^{-1}$ Mpc, grid size $N^3 = 8640^3$, FDM mass $mc^2 = 7 \times 10^{-23}$ eV (left), and in a similar CDM simulation with 2048^3 particles (right). In order to enable `DISPERSE` to process the simulated density field, it had to be scaled down to a 288^3 (FDM) or 260^3 (CDM) grid.

in a reasonable filament catalogue which traces a good fraction of the cosmic web, as shown in [Fig. 9](#).

While it is of course possible to investigate quantities like the radial filament density profiles even with this degraded resolution, the results are not very insightful since the identified filament lines will not generally trace the true, fully-resolved filament centres, making the computed profiles in a significant fraction of the total radial extent unreliable due to the varying offsets from the centre. In order to improve our measurement, we post-processed the filaments output by `DISPERSE` by evaluating each filament segment and gradually shrinking a cylindrical region around the segment towards the centre of mass contained within the region at each step, similar to the ‘shrinking spheres’ technique often used to determine the densest (central) point of a halo. In this case, the segments were only allowed to be offset in a direction perpendicular to themselves, in order to avoid several segments clustering around a single dense point and preserving the

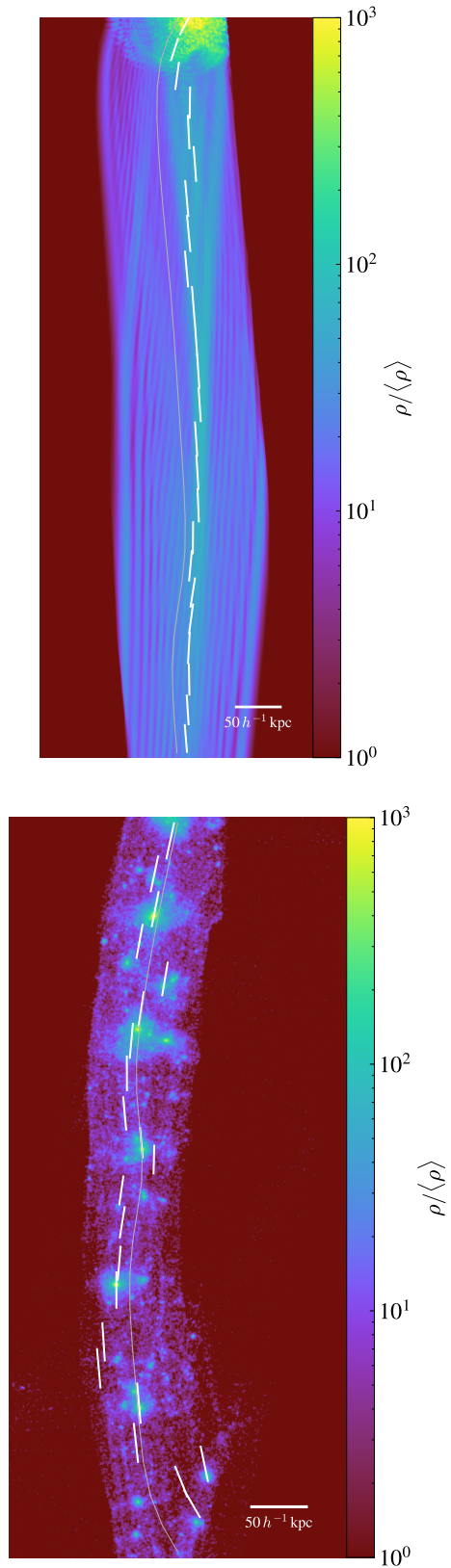


Figure 10. Projected dark matter density for an example FDM (top) and CDM (bottom) filament. A thin grey line indicates the location as identified by DisPerSE on the coarse grid, while the thicker white line segments show how this initial DisPerSE output was shifted to more accurately capture the filament centre for the purposes of computing radial density profiles.

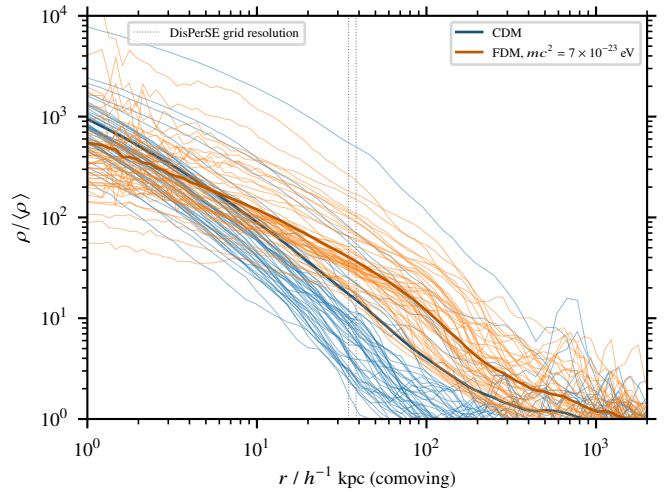


Figure 11. Filament profiles at $z = 3$ for the filaments identified by DisPerSE in $L = 10 h^{-1}$ Mpc cosmological box simulations of CDM (2048^3 particles) and FDM ($N^3 = 8640^3$, $m_c^2 = 7 \times 10^{-23}$ eV), scaled down to 260^3 and 288^3 grids, respectively, for processing with DisPerSE. The corresponding grid resolutions used with DisPerSE are marked by dashed lines. Filaments identified by DisPerSE were post-processed using the full simulation data, allowing to resolve the density profiles at much smaller distances than the resolution imposed by the DisPerSE grids. The thin lines show a random sample of individual filament profiles, while the thick lines are the mean ("stacked") density profiles of all filaments with a total length $> 350 h^{-1}$ kpc.

property that the segments trace the full length of the filament. While they do not remain continuously connected with this approach, the resulting error in the density profiles will be rather small as long as the originally identified filament line roughly traces the actual filament, since there will only be a slight inaccuracy in the measured distances of matter from the line centre due to the tilt of the segments compared to the "true" continuous filament line.

Selected FDM and CDM filaments are shown in Fig. 10, demonstrating the outcome of this procedure. Especially for FDM, it can clearly be seen that the original line which runs offset from the densest inner region of the filament is correctly shifted towards the centre. For CDM, on the other hand, the definition of a filament centre is more problematic, since the filaments are peppered with numerous small haloes, which are locally the densest points. While the procedure also correctly shifts the segments to these dense points, the set of segments can become quite discontinuous in this case, and it is visually not clear that the haloes trace what one would intuitively identify as the centre of the filament as a whole. It may be the case that another tracer, such as a suitably smoothed halo distribution, is more appropriate to describe the shape of CDM filaments.

The final (cylindrically) radial density profiles, both as "stacked" profiles and for a sample of individual ones, can be found in Fig. 11. It is evident that, for both FDM and CDM, filaments can reach rather high central densities. The main difference between the two is the slope and extent of the density profiles: The FDM filament density remains relatively flat and falls more slowly towards the outer regions, reaching much further outwards before dropping to the background matter density, while CDM filament profiles are relatively steep. Whereas CDM filaments on average decline around a radius of $500 h^{-1}$ kpc, FDM ones often extend beyond $1 h^{-1}$ Mpc.

In the inner regions, CDM filaments seem to reach higher central densities, although this statement should be interpreted with caution. Firstly, as mentioned before, it should not be expected that the identified filaments represent the full population present in the

simulation due to the coarse-graining which had to be performed on the density fields. Secondly, the grid resolution for the FDM simulation fundamentally limits the scales on which the density profile can be measured, whereas CDM particles can gather on much smaller scales, so the innermost regions may be subject to resolution effects. Thirdly, the filament segments tend to centre on haloes present in the CDM filaments, which of course tend to have very high inner densities, meaning that the density profile measurement is in part "contaminated" by these halo profiles. This once again raises the question of how to define the filament centre. Finally, the scatter in FDM filament densities is much greater than for CDM, in particular featuring a population of filaments with inner densities of around $10^{-2}\rho_m$ or even below. Further investigation into different populations of filaments may reveal why these only seem to occur with FDM. Another interesting observation is that the inner FDM filament profiles are much noisier than the CDM ones. While this can be partially attributed to resolution, which leads to poor sampling rates in the small inner cylindrical shells, it could also be a hint of the wave patterns and fluctuations present with FDM.

Generally, it is clear that our procedure employed here is not the ideal way to measure dark matter filaments. However, in the absence of superior methods and tools, Fig. 11 demonstrates that it can still provide adequate results even far below the nominal grid resolution. The main drawback of the approach is that the filament population, as identified by DISPERSE on the coarse density grids, is likely incomplete, leading to potential biases in quantities like the mean density profiles. Further, the sample is contaminated by pathological cases, such as spurious filaments which do not directly correspond to any structure in the original, fine density field. Unfortunately, the need for "correcting" the output in post-processing makes it difficult to distinguish legitimate cases which can be fixed from pathological ones. Enforcing a minimal filament length somewhat alleviates this, but is not a complete solution.

7 FUZZY DARK MATTER HALO PROFILES FROM A SELF-CONSISTENT COSMOLOGY

The halo catalogues from our simulations in May & Springel (2021) are also very useful to study a large sample of FDM haloes, e. g. in the context of the core–halo mass relation (Chan et al. 2022). Due to the use of a CDM initial matter power spectrum, the HMF is strongly enhanced compared to a ‘pure’ self-consistent FDM model, even for low halo masses, as shown in section 5. This significantly boosts the statistics by increasing the number of simulated haloes by several orders of magnitude, which can alleviate the issue of limited simulation volumes available in FDM simulations to some extent.

However, there is the lingering question of whether the cosmological context, which differs from that of a ‘real’ FDM cosmology due to the use of a CDM initial matter power spectrum, has an impact on the halo properties, and thus whether this approach is ultimately valid for studying halo profiles. If this was the case, then the halo population may not be representative of a true sample of FDM haloes with self-consistent ICs, making the approach less suitable for studying FDM halo properties. With the addition of FDM IC simulations of sufficient size, we are now able to explicitly check for differences in halo properties for the different ICs.

In Fig. 12, we show the radial density profile of all haloes in the largest FDM simulation, as well as the ‘stacked’ profile defined by

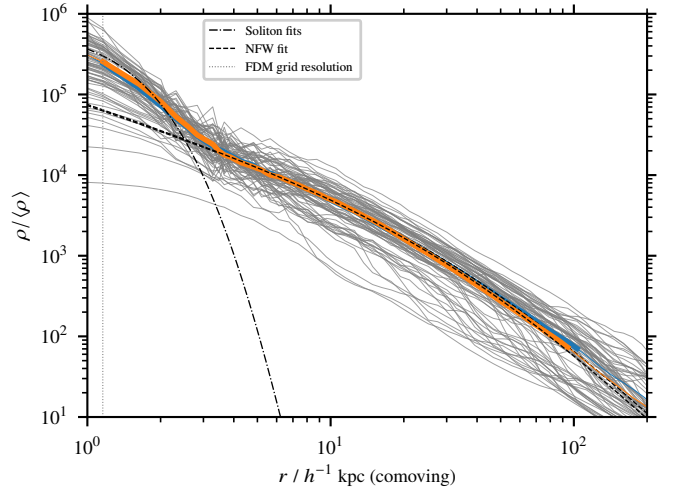


Figure 12. Halo profiles for all 68 identified haloes (grey lines) in an $L = 10 h^{-1}$ Mpc cosmological box simulation of FDM ($N^3 = 8640^3$, $mc^2 = 7 \times 10^{-23}$ eV, FDM ICs). Additionally, the coloured lines show the ‘stacked’ profile of all haloes for the FDM IC case and the subset of haloes which match these most closely in mass for the CDM IC case. The thin dashed line shows an Navarro–Frenk–White (NFW) fit (eq. (26)) to the region of the stacked profile within the virial radius R_{200} , which is indicated with a thick line.

these haloes.¹⁰ In order to compare to the simulation with CDM ICs, which contains many more haloes, we selected an equal number of haloes which most closely match those in the FDM IC simulation. The resulting stacked profile is also plotted in Fig. 12, with both stacked profiles matching excellently – presenting a solitonic core in the centre and the familiar Navarro–Frenk–White (NFW) density profile (Navarro et al. 1996, 1997),

$$\rho_{c,\text{NFW}}(r_c) = \frac{\rho_0}{\frac{r_c}{R_s} \left(1 + \frac{r_c}{R_s}\right)^2} \quad (26)$$

in the outskirts. Thus, while there might certainly be a statistical impact in the form that a larger sample of haloes is more likely to contain outliers, e. g. ‘unusual’ haloes with a ‘rare’ merger history, both cases agree very well at the level of the averaged density profiles, and our results do not show evidence for any systematic differences.

8 SUMMARY AND CONCLUSIONS

The simulations presented in this work constitute the largest numerical simulations of cosmic structure formation with FDM that account for its full wave nature via the SP equations, using a pseudo-spectral method. By approaching simulation volumes more representative of cosmic large-scale structure, we have been able to follow the combined linear large-scale, and non-linear small-scale evolution of wave FDM in a fully self-consistent manner. The pseudo-spectral method can be considered the most accurate approach to solve the SP system of equations numerically (although usually, the issue is not about the accuracy of the numerical approach to SP equations, but rather whether an attempt is made to solve these equations at all, or whether the cost is shirked by choosing one of the approximate options). It encompasses all aspects of the wave amplitude’s temporal evolution,

¹⁰ The procedure of ‘stacking’ refers to taking the mean density across all haloes for each radial bin.

and in particular accounts for the oscillatory, order-unity fluctuations of the local density due to the wave effects in the axion-like dynamics.

We stress again that, unfortunately, the numerical resolution requirements to faithfully follow the FDM dynamics are much more stringent than for the familiar N -body techniques applicable in the CDM case. Even large-scale modes require a very fine mesh due to the velocity criterion, eq. (17), since the spatial oscillations of the phase factors are otherwise not resolved, resulting in a halted evolution and eventually just numerical noise. Nevertheless, the time step criterion, eq. (15), with its quadratic (rather than linear) dependence on the spatial resolution, enforces very small time steps when the mesh is made fine enough to resolve the de Broglie wavelength λ_{dB} , even when the coarsest possible mesh resolution is selected. These requirements continue to severely limit the regimes available to full numerical simulations of FDM, and in particular preclude large cosmological volumes to be computed at low resolution in a way similar to the standard practice in CDM.

The large, fully self-consistent FDM simulations we have performed here have allowed us to gain new insights into the evolution of the non-linear power spectrum in these cosmologies, especially in comparison to CDM and the simplified approach of ‘CDM with FDM ICs’. We could also make the first direct, self-consistent measurements of the halo mass function in such models. In the process, we have discovered that the filamentary structure of the cosmic web behaves more similarly to WDM than to CDM, and we have characterised the properties of these filaments in comparison to CDM.

Our main findings can be summarized as follows:

- Our study could determine the fully non-linear matter power spectrum of self-consistently evolved FDM cosmologies over an exceptionally broad range of scales, and we have also computed matching CDM N -body simulations with the same initial conditions. On large scales, we confirmed the consistency between all simulations – a manifestation of the Schrödinger–Poisson–Vlasov–Poisson correspondence, verifying the expectation that FDM behaves like CDM on these scales. On small scales, the ‘quantum pressure’ in FDM suppresses structure formation compared to CDM. Self-consistently accounting for FDM yields initial conditions with substantially reduced power on small scales, however, producing yet bigger suppression effects for small-small haloes, in a way strongly reminiscent of WDM models.

- We were able to draw a four-way comparison of the evolution of the matter power spectrum for the different choices of simulated dynamics and ICs. Our findings demonstrate that the differences between each option are time-dependent, with large variations in their relative behaviours. Especially at early times, the ICs are the determining factor, dominating the shape of the power spectrum at small scales due to the cut-off from at the FDM Jeans scale. By $z = 15$, bottom-up structure formation is already in full swing for CDM, with non-linear excess power accumulating on small scales. FDM with CDM ICs starts to reach the linear theory power spectrum again at this point, whereas simulations with FDM ICs are still significantly lagging behind on scales smaller than the initial cut-off. Finally, for smaller redshifts, the shapes of all power spectra start to become rather similar, and by $z = 3$, the impact of going from CDM to FDM ICs and from N -body to SP dynamics is roughly similar in size. Of course, only SP simulations exhibit a small-scale excess ‘bump’ (exceeding even the CDM power) due to wave interference.

- We have developed a technique which allows us to reliably identify haloes in self-consistent FDM SP simulations, including the proper ‘WDM-like’ ICs with suppressed small-scale power. This proved non-trivial because, similar to WDM, standard halo finding

algorithms like FoF are not able to handle on their own the presence of extended, smoothly overdense filaments. By employing an increased overdensity threshold combined with a binding criterion and a filter on the identified objects’ virial ratios, we have been able to identify the subset of gravitationally collapsed, virialised objects.

- We could, for the first time, measure the self-consistent halo mass function directly from pseudo-spectral FDM simulations. By comparing SP simulations with FDM and CDM ICs, we could confirm that the FDM ICs have a larger impact on the HMF than the late-time non-linear SP dynamics, although the suppression caused by the latter is still significant. For the ‘true’ FDM HMF, we find broad agreement with the approximate scheme of obtaining the HMF from N -body simulations with an FDM power spectrum (‘CDM with FDM ICs’). In contrast, predictions based on the extended Press–Schechter formalism (Du et al. 2017; Kulkarni & Ostriker 2022) do not fit our HMF results so well.

- We have investigated the differences between cosmic filaments for FDM and CDM. Like WDM, FDM filaments do not fragment into (sub-)haloes like those of CDM, and instead feature the characteristic wave fluctuation patterns. We found significant differences in the shapes of filamentary density profiles, with FDM filaments being much more extended and with a more slowly-declining density than CDM ones. The scatter in identified filaments was also larger for FDM, which features a population with very high densities (even comparable to lower-mass haloes). Such objects have been found to be the sites of first star formation with FDM (Mocz et al. 2020).

- One advantage of the ‘FDM with CDM ICs’ simulations which we have performed previously is the much larger population of simulated haloes, which can be used to infer FDM halo properties using a large sample. However, it has not been a priori clear whether all the haloes obtained in such a simulation are representative of a fully self-consistent FDM cosmology that is based on the correct primordial power spectrum, yielding only a much suppressed halo abundance. In this work, we have been able to show that the properties of the simulated haloes match quite closely, validating the use of the larger halo catalogues for the purposes of studying FDM haloes. This is reminiscent of N -body simulations of CDM and WDM cosmologies, which show very similar halo density profiles apart from a slightly reduced concentration of WDM haloes, consistent with their later formation time (Avila-Reese et al. 2001).

Cosmological simulations of FDM are numerically much more challenging than CDM, but our work shows that at least small volumes can be studied with decent spatial resolution. Including baryons explicitly would clearly be a very worthwhile and interesting next step to arrive at a more reliable assessment of whether these cosmologies are still viable, and how tight some of the constraints placed on the particle mass really are. In this regard, the high computational cost of FDM simulations can actually be viewed as an encouragement. Unlike for ‘cheap’ CDM simulations, adding hydrodynamics and a modelling of galaxy formation physics should be comparatively easy to do – at least it is not expected to dominate the computational expense, and in this sense appears quite feasible. We intend to attempt this in forthcoming work.

ACKNOWLEDGEMENTS

The authors would like to thank Daniela Galárraga-Espinosa for her help with the use of `DISPERSE`, and Jens Stücker for a helpful discussion about methods for halo identification, as well as Mihir Kulkarni and Xiaolong Du for providing code to calculate the HMF using their methods. Computations were performed on the high-performance

computing (HPC) systems Cobra, Raven, and Freya at the Max Planck Computing and Data Facility (MPCDF).¹¹

AXI REPO (and AREPO) make use of the FFTW (Frigo & Johnson 2005), GSL (Galassi et al. 2009), and HDF5 (HDF Group 2022) libraries. We employed the GCC (GNU Project 2022) and OPEN MPI (Gabriel et al. 2004) implementations of the C programming language and the MPI standard. The following software and libraries were additionally used for data analysis and production of figures: PYTHON (van Rossum 1995; Python Software Foundation 2022), NUMPY (Harris et al. 2020), SCIPY (Virtanen et al. 2020), NUMBA (Lam et al. 2015), MATPLOTLIB (Hunter 2007), MPI4PY (Dalcin et al. 2005; Dalcin & Fang 2021), ASTROPY (Greenfield et al. 2013; Astropy Collaboration et al. 2018), YT (yt project 2010; Turk et al. 2011).

DATA AVAILABILITY

The data underlying this article will be shared upon reasonable request to the corresponding author.

REFERENCES

- Angulo R. E., Hahn O., Abel T., 2013, *MNRAS*, **434**, 3337
- Astropy Collaboration et al., 2018, *AJ*, **156**, 123
- Avila-Reese V., Colín P., Valenzuela O., D’Onghia E., Firmani C., 2001, *ApJ*, **559**, 516
- Barnes J. E., Hut P., 1989, *ApJS*, **70**, 389
- Bett P., Eke V., Frenk C. S., Jenkins A., Helly J., Navarro J., 2007, *MNRAS*, **376**, 215
- Boyersky A., Drewes M., Lasserre T., Mertens S., Ruchayskiy O., 2019, *Progress in Particle and Nuclear Physics*, **104**, 1
- Boylan-Kolchin M., Bullock J. S., Kaplinghat M., 2011, *MNRAS*, **415**, L40
- Bull P., et al., 2016, *Physics of the Dark Universe*, **12**, 56
- Burkert A., 2020, *ApJ*, **904**, 161
- Chan H. Y. J., Ferreira E. G. M., May S., Hayashi K., Chiba M., 2022, *MNRAS*, **511**, 943
- Dalal N., Kravtsov A., 2022, arXiv e-prints, p. arXiv:2203.05750
- Dalcin L., Fang Y.-L. L., 2021, *Computing in Science & Engineering*, **23**, 47
- Dalcin L., Paz R., Storti M., 2005, *Journal of Parallel and Distributed Computing*, **65**, 1108
- Del Popolo A., Le Delliou M., 2017, *Galaxies*, **5**, 17
- Despali G., Giocoli C., Angulo R. E., Tormen G., Sheth R. K., Baso G., Moscardini L., 2016, *MNRAS*, **456**, 2486
- Du X., Behrens C., Niemeyer J. C., 2017, *MNRAS*, **465**, 941
- Efstathiou G., Sutherland W. J., Maddox S. J., 1990, *Nature*, **348**, 705
- Efstathiou G., Bond J. R., White S. D. M., 1992, *MNRAS*, **258**, 1P
- Ferreira E. G. M., 2021, *A&ARv*, **29**, 7
- Frenk C. S., White S. D. M., 2012, *Annalen der Physik*, **524**, 507
- Frigo M., Johnson S., 2005, *Proceedings of the IEEE*, **93**, 216
- GNU Project 1987–2022, The GNU Compiler Collection, <https://gcc.gnu.org/>
- Gabriel E., et al., 2004, in Proceedings, 11th European PVM/MPI Users’ Group Meeting. Budapest, Hungary, pp 97–104
- Galárraga-Espinosa D., Aghanim N., Langer M., Gouin C., Malavasi N., 2020, *A&A*, **641**, A173
- Galassi M., Davies J., Theiler J., Gough B., Jungman G., 2009, GNU scientific library reference manual, 3 edn. Network Theory, Bristol, <https://www.gnu.org/software/gsl/>
- Gao L., Theuns T., 2007, *Science*, **317**, 1527
- Gao L., Theuns T., Springel V., 2015, *MNRAS*, **450**, 45
- Grand R. J. J., et al., 2021, *MNRAS*, **507**, 4953
- Greenfield P., et al., 2013, Astropy: Community Python library for astronomy, Astrophysics Source Code Library, record ascl:1304.002
- Grin D., Marsh D. J. E., Hložek R., 2022, axionCAMB: Modification of the CAMB Boltzmann code, Astrophysics Source Code Library, record ascl:2203.026
- Gross E. P., 1961, *Il Nuovo Cimento*, **20**, 454
- HDF Group 1997–2022, Hierarchical Data Format, version 5, <https://www.hdfgroup.org/HDF5/>
- Harris C. R., et al., 2020, *Nature*, **585**, 357
- Hayashi K., Ferreira E. G. M., Chan H. Y. J., 2021, *ApJ*, **912**, L3
- Hellwing W. A., Schaller M., Frenk C. S., Theuns T., Schaye J., Bower R. G., Crain R. A., 2016, *MNRAS*, **461**, L11
- Hložek R., Grin D., Marsh D. J. E., Ferreira P. G., 2015, *Phys. Rev. D*, **91**, 103512
- Hu W., Barkana R., Gruzinov A., 2000, *Phys. Rev. Lett.*, **85**, 1158
- Hui L., 2021, *ARA&A*, **59**, 247
- Hui L., Ostriker J. P., Tremaine S., Witten E., 2017, *Phys. Rev. D*, **95**, 043541
- Hui L., Joyce A., Landry M. J., Li X., 2021, *J. Cosmology Astropart. Phys.*, **2021**, 011
- Hunter J. D., 2007, *Computing in Science & Engineering*, **9**, 90
- Jenkins A., et al., 1998, *ApJ*, **499**, 20
- Jenkins A., Frenk C. S., White S. D. M., Colberg J. M., Cole S., Evrard A. E., Couchman H. M. P., Yoshida N., 2001, *MNRAS*, **321**, 372
- Kulkarni M., Ostriker J. P., 2022, *MNRAS*, **510**, 1425
- Lagué A., Bond J. R., Hložek R., Marsh D. J. E., Söding L., 2021, *MNRAS*, **504**, 2391
- Lam S. K., Pitrou A., Seibert S., 2015, in Proceedings of the Second Workshop on the LLVM Compiler Infrastructure in HPC. LLVM ’15. Association for Computing Machinery, New York, NY, USA, doi:10.1145/2833157.2833162, <https://numba.pydata.org/>
- Li X., Hui L., Bryan G. L., 2019, *Phys. Rev. D*, **99**, 063509
- Lovell M. R., Frenk C. S., Eke V. R., Jenkins A., Gao L., Theuns T., 2014, *MNRAS*, **439**, 300
- Madelung E., 1927, *Zeitschrift für Physik*, **40**, 322
- Marsh D. J. E., 2016, *Phys. Rep.*, **643**, 1
- Marsh D. J. E., Silk J., 2014, *MNRAS*, **437**, 2652
- May S., Springel V., 2021, *MNRAS*, **506**, 2603
- Mocz P., Vogelsberger M., Robles V. H., Zavala J., Boylan-Kolchin M., Fialkov A., Hernquist L., 2017, *MNRAS*, **471**, 4559
- Mocz P., Lancaster L., Fialkov A., Becerra F., Chavanis P.-H., 2018, *Phys. Rev. D*, **97**, 083519
- Mocz P., et al., 2020, *MNRAS*, **494**, 2027
- Navarro J. F., Frenk C. S., White S. D. M., 1996, *ApJ*, **462**, 563
- Navarro J. F., Frenk C. S., White S. D. M., 1997, *ApJ*, **490**, 493
- Neto A. F., et al., 2007, *MNRAS*, **381**, 1450
- Niemeyer J. C., 2020, *Progress in Particle and Nuclear Physics*, **113**, 103787
- Nori M., Baldi M., 2018, *MNRAS*, **478**, 3935
- Nori M., Baldi M., 2021, *MNRAS*, **501**, 1539
- Nori M., Murgia R., Iršič V., Baldi M., Viel M., 2019, *MNRAS*, **482**, 3227
- Pitaevskii L. P., 1961, *Journal of Experimental and Theoretical Physics*, **13**, 451
- Press W. H., Schechter P., 1974, *ApJ*, **187**, 425
- Python Software Foundation 2001–2022, The Python Programming Language, <https://www.python.org/>
- Sales L. V., Wetzel A., Fattahi A., 2022, *Nature Astronomy*, **6**, 1000
- Santos-Santos I. M. E., et al., 2020, *MNRAS*, **495**, 58
- Shive H.-Y., Chiueh T., Broadhurst T., 2014, *Nature Physics*, **10**, 496
- Shive H.-Y., Chiueh T., Broadhurst T., Huang K.-W., 2016, *ApJ*, **818**, 89
- Schwabe B., Niemeyer J. C., 2022, *Phys. Rev. Lett.*, **128**, 181301
- Sheth R. K., Tormen G., 1999, *MNRAS*, **308**, 119
- Sousbie T., 2011, *MNRAS*, **414**, 350
- Sousbie T., Pichon C., Kawahara H., 2011, *MNRAS*, **414**, 384
- Springel V., 2010, *MNRAS*, **401**, 791
- Springel V., 2015, N-GenIC: Cosmological structure initial conditions, Astrophysics Source Code Library, record ascl:1502.003
- Springel V., et al., 2018, *MNRAS*, **475**, 676
- Stücker J., Angulo R. E., Busch P., 2021, *MNRAS*, **508**, 5196

¹¹ <https://www.mpcdf.mpg.de/>

- Tinker J., Kravtsov A. V., Klypin A., Abazajian K., Warren M., Yepes G., Gottlöber S., Holz D. E., 2008, *ApJ*, 688, 709
- Tulin S., Yu H.-B., 2018, *Phys. Rep.*, 730, 1
- Turk M. J., Smith B. D., Oishi J. S., Skory S., Skillman S. W., Abel T., Norman M. L., 2011, *ApJS*, 192, 9
- Veltmaat J., Niemeyer J. C., 2016, *Phys. Rev. D*, 94, 123523
- Veltmaat J., Niemeyer J. C., Schwabe B., 2018, *Phys. Rev. D*, 98, 043509
- Virtanen P., et al., 2020, *Nature Methods*, 17, 261
- Vogelsberger M., Marinacci F., Torrey P., Puchwein E., 2020, *Nature Reviews Physics*, 2, 42
- Wang J., White S. D. M., 2007, *MNRAS*, 380, 93
- Weinberg D. H., Bullock J. S., Governato F., Kuzio de Naray R., Peter A. H. G., 2015, *Proceedings of the National Academy of Science*, 112, 12249
- Widrow L. M., Kaiser N., 1993, *ApJ*, 416, L71
- Woo T.-P., Chiueh T., 2009, *ApJ*, 697, 850
- Zhang J., Liu H., Chu M.-C., 2018a, *Frontiers in Astronomy and Space Sciences*, 5, 48
- Zhang J., Kuo J.-L., Liu H., Sming Tsai Y.-L., Cheung K., Chu M.-C., 2018b, *ApJ*, 863, 73
- Zoutendijk S. L., Brinchmann J., Bouché N. F., den Brok M., Krajnović D., Kuijken K., Maseda M. V., Schaye J., 2021, *A&A*, 651, A80
- van Rossum G., 1995, Technical Report CS-R9525, Python Reference Manual. Centrum voor Wiskunde en Informatica, Amsterdam
- yt project 2010, yt: A Multi-Code Analysis Toolkit for Astrophysical Simulation Data, Astrophysics Source Code Library, record ascl:1011.022

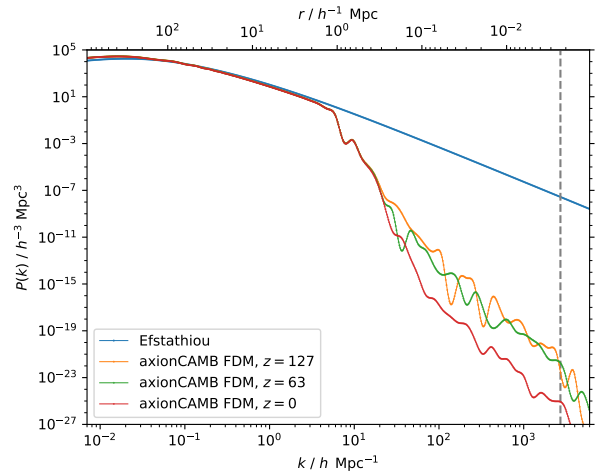


Figure A1. Linear FDM power spectra ($mc^2 = 7 \times 10^{-23}$ eV) generated by `AXIONCAMB` for different redshifts z , with the Efstathiou et al. (1990, 1992) power spectrum from eq. (21) for comparison. For easier comparison, all power spectra were scaled to $z = 0$ using the linear CDM growth factor. The dashed vertical line indicates the grid resolution scale for a simulation in a $10 \text{ Mpc } h^{-1}$ box with an 8640^3 grid.

APPENDIX A: SMALL INCONSISTENCY IN THE FUZZY DARK MATTER INITIAL CONDITIONS

After performing the simulations with FDM ICs, we discovered that, unfortunately, a small error had occurred with the used input power spectra (generated by `AXIONCAMB`): Instead of generating the power spectrum at the correct starting redshift of $z = 127$, the power spectrum was generated for $z = 0$ and then scaled back to $z = 127$ using the (scale-independent) CDM growth factor. However, since the growth factor for FDM is scale-dependent, procedure does not result in the correct power spectrum for an earlier redshift.

Fig. A1 shows how the shape of the linear FDM power spectrum compares for different redshifts. In this case, the red line ($z = 0$) was used (incorrectly) instead of the orange line ($z = 127$). Fortunately, the discrepancy is not very serious. Since FDM coincides with CDM on large scales, there is no error incurred there. The difference essentially boils down to a slightly increased suppression on scales smaller than $300 h^{-1}$ kpc, accompanied by some changes in the details of the oscillations of the power spectrum on these scales. However, the order of magnitudes of the relative suppression involved (compared to CDM) are 10^{-12} and 10^{-9} , or in other words, structure is effectively completely suppressed on these scales in both cases. For all intents and purposes, the difference is negligible, and is erased by the vastly larger amount of power coming in from non-linear power transfer in the later stages of evolution (cf. section 4). Nevertheless, we would like to note this slight inconsistency in the ICs here for completeness.

This paper has been typeset from a \LaTeX file prepared by the author.